Quenching of O2(b1Σg+) by O(3P) atoms. Effect of gas temperature

Jean-Paul Booth, A Chatterjee, O Guaitella, D Lopaev, S Zyryanov, A Volynets, T Rakhimova, D Voloshin, A Chukalovsky, Yu. Mankelevich, et al.

Quenching of $O_2(b^1\Sigma_g^+)$ by $O(^3P)$ atoms. Effect of gas temperature.

J.P. Booth[1], A. Chatterjee[1], O. Guaitella[1], D. Lopaev[2], S. Zyryanov[2], A.Volynets[2], T. Rakhimova[2], D. Voloshin[2], A. Chukalovsky[2], Yu. Mankelevich[2], V. Guerra[3]

[1]*Laboratoire de Physique des Plasmas, CNRS, Ecole Polytechnique, UPMC Univ Paris 06, Univ Paris-Sud, France*

[2]*Skobeltsyn Institute of Nuclear Physics, Lomonosov Moscow State University, Russian Federation*

[3]*Instituto de Plasmas e Fusão Nuclear, Instituto Superior Técnico, Universidade de Lisboa, Portugal*

abstract

We present a detailed study of the density and kinetics of $O_2(b^1\Sigma_g^+)$ in steady-state and partially-modulated DC positive column discharges in pure O_2 for gas pressures of 0.3-10 Torr and 10-40 mA current. The time-resolved density of $O_2(b^1\Sigma_g^+)$ was determined by absolutely-calibrated optical emission spectroscopy (OES) of the A-band emission at 762 nm. Additionally, the $O_2(b^1\Sigma_g^+)$ density was determined by VUV absorption spectroscopy using the Fourier –Transform spectrometer at the DESIRS beamline at Synchrotron Soleil, allowing the absolute calibration of OES to be confirmed. The $O(^3P)$ atoms were detected by time-resolved sub-Doppler cavity ringdown spectroscopy (CRDS) using the $O(^3P_2) \rightarrow O(^1D_2)$ transition at 630 nm. The CRDS measurements were synchronized to the discharge modulation allowing the $O(^3P)$ dynamics to be observed. As a function of gas pressure the $O_2(b^1\Sigma_g^+)$ density passes through a maximum at about 2 Torr. Below this maximum, the $O_2(b^1\Sigma_g^+)$ density increases with discharge current, whereas above this maximum it decreases with current. The gas temperature increases with pressure and current, from 300 to 800 K. These observations can only be explained by the existence of fast quenching process of $O_2(b^1\Sigma_g^+)$ by $O(^3P)$, with a rate that increases strongly with gas temperature, i.e. with a significant energy barrier. The data are interpreted using a 1D self-consistent model of the O_2 discharge. The best fit of this model to all experimental data (including the $O_2(b^1\Sigma_g^+)$ average density as a function of pressure and current, the radial profiles, and the temporal response to current modulation) is achieved using a rate constant of $k_Q=10^{-10}\cdot\exp(-3700/T)$ cm^3/s.

1. Introduction

Non-thermal plasmas containing oxygen have been studied for many decades. They have numerous technological applications [1, 2], such as plasma surface treatments and ozonizers [3-5], gas lasers [6-11], plasma assisted combustion [12-15], and (more recently) in biology and medicine [1, 16, 17]. Therefore, one might assume that all fundamental questions concerning oxygen plasmas have been resolved, and that the kinetic reaction scheme is well established, at least concerning the basic reactions that directly affect the state of the plasma [18-25]. The principal species present include $O_2(X^3\Sigma_g^-, v)$ ground state oxygen molecules, $O(^3P)$ atoms and ozone, as well as excited metastable atoms ($O(^1D)$) and molecules ($O_2(a^1\Delta_g)$ and $O_2(b^1\Sigma_g^+)$). However, several important processes are poorly known or even not studied at all. This is especially true for reactions involving metastable molecules and oxygen atoms. For example, in a recent work by Volynets at al. [26], the existence of rapid reactive quenching of $O_2(a^1\Delta_g)$ molecules by $O(^3P)$ atoms was demonstrated experimentally for the first time. Indeed, in oxygen plasmas at elevated temperatures this process controls the population of $O_2(a^1\Delta_g)$. They explained their observations by the existence of a reactive quenching process of $O_2(a^1\Delta_g)$ by $O(^3P)$ atoms, occurring via the formation of an activated O_3^{**} complex, with an activation barrier in the range of 0.56-0.69eV. Volynets et al. also showed that a similar quenching process can occur for the $O_2(b^1\Sigma_g^+)$ state. However, the experimental conditions used in this study did not allow the rate constant and the activation barrier to be determined accurately.

This work presents a detailed study of the quenching of $O_2(b^1\Sigma_g^+)$ molecules by $O(^3P)$ atoms over a lower temperature range of 300-800K. A DC positive column discharge in oxygen (p = 0.3 - 10 Torr) allowed this process to be observed under well-controlled conditions. Kinetic measurements were made during partial modulation of the discharge current. The modulation depth and period were varied so as to clearly observe the dynamics of the $O_2(b^1\Sigma_g^+)$ and $O(^3P)$ concentrations. The temporal dynamics of the $O_2(b^1\Sigma_g^+)$ density were measured by absolutely-calibrated emission spectroscopy of the A-band, $O_2(b^1\Sigma_g^+,v=0) \rightarrow O_2(X^3\Sigma_g^-,v=0)$, at 762 nm. The absolute density and temporal dynamics of $O(^3P)$ atoms was determined by time-resolved CRDS method [27]. Comparison of the experimental results to our 1D self-consistent discharge model showed that the results can only be explained by the inclusion of a rapid quenching process of $O_2(b^1\Sigma_g^+)$ molecules by $O(^3P)$ atoms with a significant energy barrier. Moreover, the complete set of experimental data, including the dependency of the $O_2(b^1\Sigma_g^+)$ density on pressure and current, its dynamic response to current modulation and its radial density profiles, were well described using unique rate constant, indicating a high degree of confidence in this interpretation.

This article is organized as follows. Section 2 describes the experimental setup and the diagnostic techniques employed. Section 3 describes the 1D model used. Section 4 presents the experimental results and discusses them in comparison with the model.

2. Experiment

2.1. Experimental setup

The experimental scheme is shown in figure 1. A uniform positive column dc glow discharge is created in a 20mm internal diameter borosilicate glass tube. The temperature of the tube walls was controlled by a water/ethanol mixture flowing through an outer envelope connected to a thermostatic chiller. Most measurements were made with a wall temperature of 50°C, but some data was also takeb at 5°C. The anode and cathode are comprised of hollow electrodes placed in the arms of the tubes separated by 560mm, as shown in figure 1. This allows optical measurements along the axis. The same discharge setup has been used previously for a study of $O(^3P)$ surface recombination by time-resolved actinometry [28], for time-resolved VUV absorption measurements [29], and by Western at al. [30] to measure the VUV absorption spectra of $O_2(b^1\Sigma_g^+)$ and $O_2(a^1\Delta_g)$.

The experiments were carried out in the pressure range 0.3-10 Torr and current 5-40 mA. Pure O_2 (99.999%) was flowed at 5sccm for pressures below 1 Torr and 10 sccm for pressures above 1 Torr. This ensures a long gas residence time (> 1s) so that the discharge always reaches steady-state during modulation. The concentrations of all active particles, especially the long-lived species such as $O(^3P)$ atoms and $O_2(a^1\Delta_g)$ molecules, reach stationary values. Partial modulation of the discharge current (~15%) was achieved by rapid (< 1 μs) short-circuiting of part of the ballast discharge resistance using a MOSFET transistor, which ensured a rapid change (increase and decrease) in the discharge current within a few microseconds to a new value determined by the new value of the ballast resistance. Nevertheless, the discharge current can continue to vary slightly after switching due to slow kinetic processes, mainly associated with the associative detachment of electrons from negative ions by oxygen atoms and $O_2(a^1\Delta_g)$. The modulation period was significantly longer than the time needed to reach steady state. The characteristic modulation period was about 11 ms for "fast" modulation and ~400 ms for "slow" modulation.

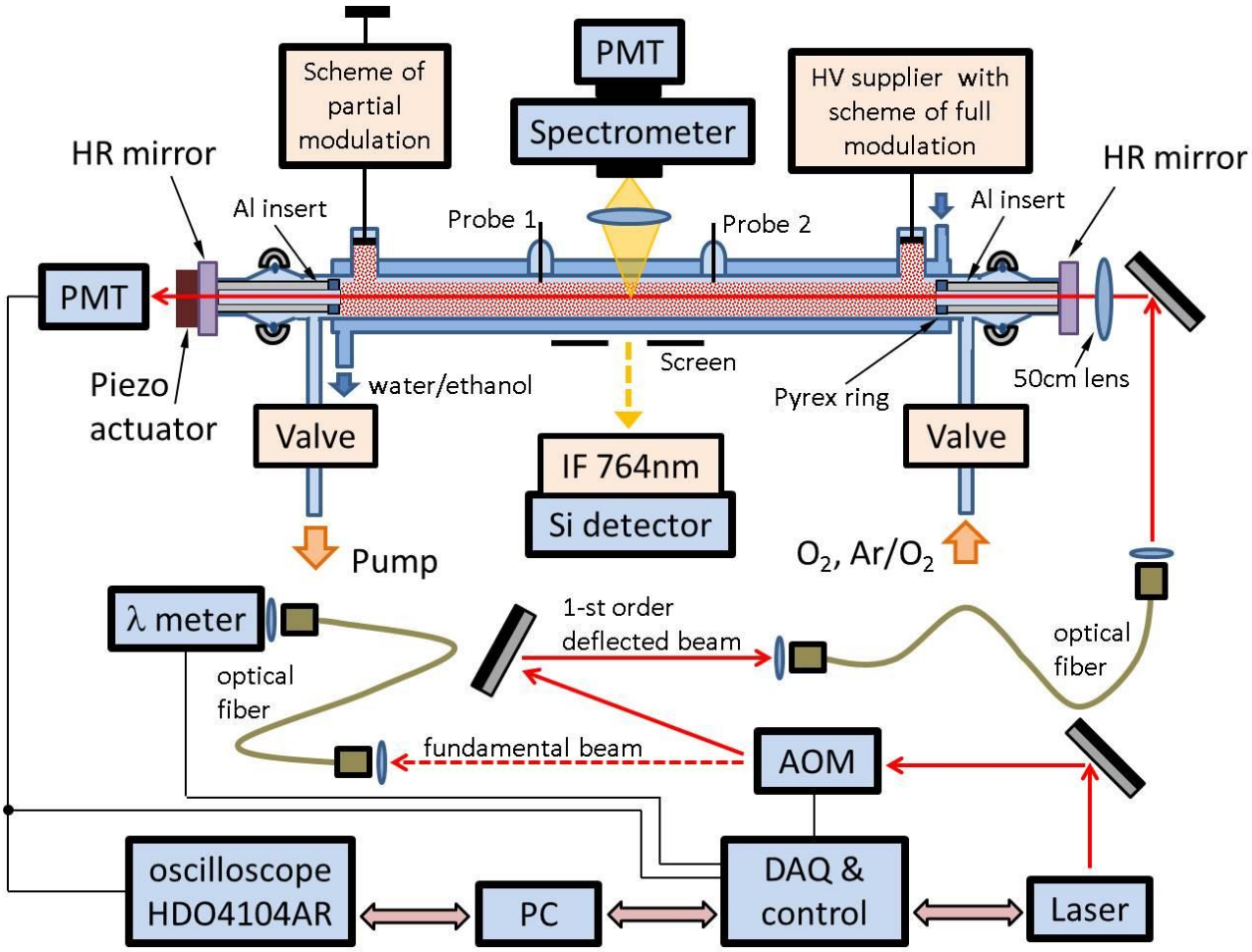

Figure 1. Experimental set up. See sections 2.2 and 2.5 for details on OES and CRDS measurements.

2.2. Measurement of $O_2(b^1\Sigma_g^+)$ by optical emission spectroscopy

The $O_2(b^1\Sigma_g^+,v=0) \rightarrow O_2(X^3\Sigma_g^-,v=0)$ A-band emission at 762 nm was detected using a spectrometer (Princeton IsoPlane SCT-320) and PMT (Hamamatsu R13456), similar to that used in Booth et al. [28]. The intensity of hot bands ($O_2(b^1\Sigma_g^+,v=1) \rightarrow O_2(X^3\Sigma_g^-,v=1)$ and $O_2(b^1\Sigma_g^+,v=2) \rightarrow O_2(X^3\Sigma_g^-,v=2)$) was lower by two orders of magnitude, which, taking into account the Franck-Condon factors, indicates a very low population of the vibrationally-excited levels of $b^1\Sigma_g^+$ state. Therefore, it was further assumed that the concentration of $O_2(b^1\Sigma_g^+)$ molecules is equal to the concentration of $O_2(b^1\Sigma_g^+,v=0)$, i.e. $[O_2(b^1\Sigma_g^+)] = [O_2(b^1\Sigma_g^+,v=0)]$.

An example of a high-resolution spectrum of A-band emission is shown in figure 2. The fine structure of the rotational lines (in the P-branch and even more so in the R-branch) was not resolved. However, this spectral resolution was sufficient to allow the rotational temperature to be determined (by fitting a simulated P-branch spectrum to the experimental one) with an accuracy of ~2-3%. At these pressures it is safe to assume that the rotational temperature is in equilibrium with the gas translational temperature, T_g,

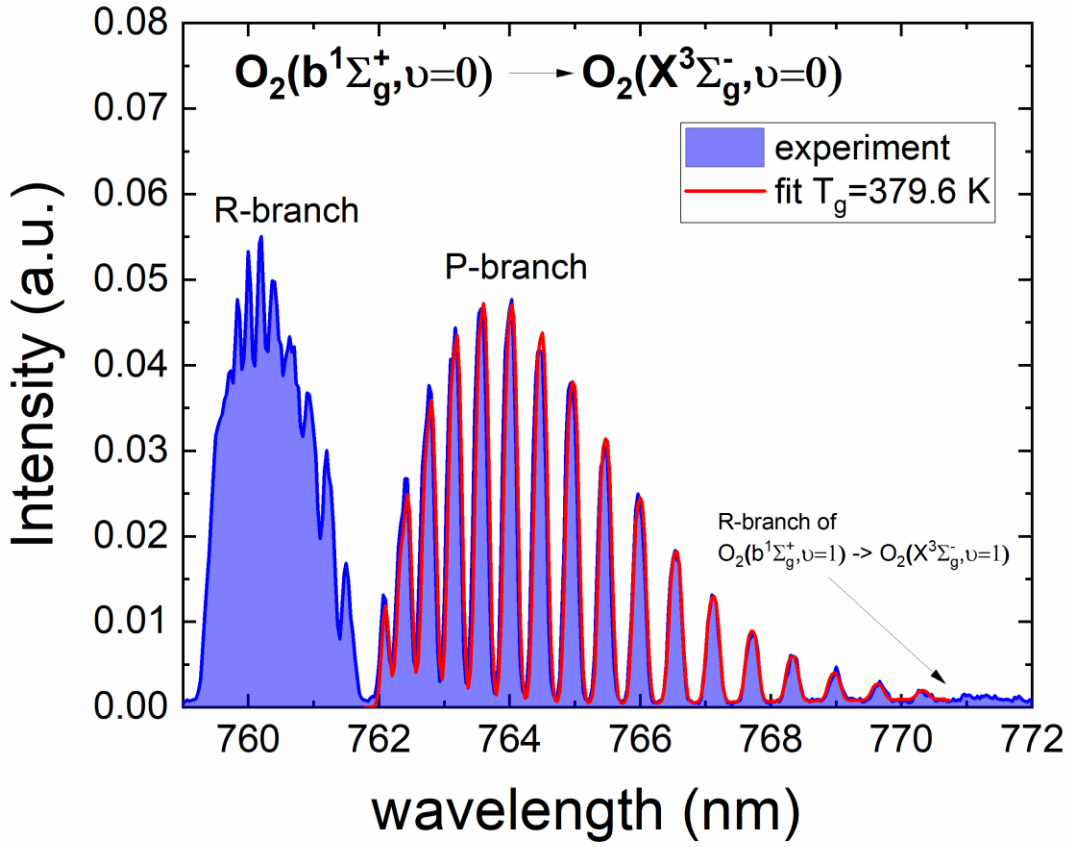

Figure 2. A-band, $O_2(b^1\Sigma_g^+,v=0) \rightarrow O_2(X^3\Sigma_g^-,v=0)$, emission spectrum at 2 Torr, 20 mA and wall temperature +5C. The blue curve is the measured spectrum. The red curve is a simulated spectrum for T_g=379.6 K.

We used two optical schemes to detect $O_2(b^1\Sigma_g^+)$ emission. In the first scheme, the $O_2(b^1\Sigma_g^+)$ emission along the discharge axis was collected via two windows installed at the tube ends, as described in Booth et al.[28]. Unfortunately, the window diameter was slightly smaller than the tube diameter, preventing detection close to the wall. The spectrometer was situated at ~2.7 m from the window (3 m from the tube center), and a 75cm FL lens was used to create an image of the tube diameter at the entrance slit of the imaging spectrometer. Light exiting the spectrometer was detected by an ICCD camera (Princeton PI-MAX 4), giving a spatial image of the A-band spectrum across the tube diameter. In this way the radial temperature profile could be determined.

In the second scheme, light emitted transverse to the tube axis from the tube center was detected. The light was collected by a short-focus lens so that the emission of almost all $O_2(b^1\Sigma_g^+)$ molecules in the selected cross-section of the tube was detected. Therefore, in this case the temperature and density are averaged over tube cross section. Thus, in this configuration the values obtained for T_g and the $O_2(b^1\Sigma_g^+)$ density is averaged over the tube radius. Compared to the axial scheme, this configuration provides better sensitivity, allowing reproducible measurements of the dynamics of the $O_2(b^1\Sigma_g^+)$ concentration during discharge modulation. To avoid sensitivity to changes in the A-band spectrum shape on the $O_2(b^1\Sigma_g^+)$ density dynamics, the integrated R-branch emission was measured using wide slits (500 microns) on the spectrometer. In this way the relative $O_2(b^1\Sigma_g^+)$ density was determined as a function of discharge conditions (O_2 pressure, current,

surface temperature) and as a function of time in kinetic measurements, and put on an absolute scale as described in the next section.

2.3. Absolute calibration of $O_2(b^1\Sigma_g^+)$ density

In order to put the relative measurements of $O_2(b^1\Sigma_g^+)$ density from the transverse emission intensity detected by the monochromator + photomultiplier, it is necessary to measure the absolute transverse emission intensity. This was done using an absolutely-calibrated Si photodiode (AXUV100G, detecting area S_{det} = 1 cm^2) with a narrow-band (~10 nm) interference filter centered at 764 nm to measure the wavelength-integrated absolute intensity of the $O_2(b^1\Sigma_g^+,v=0) \rightarrow O_2(X^3\Sigma_g^-,v=0)$ band. Figure 3a shows a typical $O_2(b^1\Sigma_g^+)$ emission spectrum (1 Torr, 20 mA), along with the transmittance curve of the interference filter (dashed line). The convolution of the filter transmittance with the A-band spectrum was calculated for all discharge conditions studied. Since the filter bandwidth is rather wide, this convolution gives an almost constant coefficient, only slightly varying with the discharge conditions.

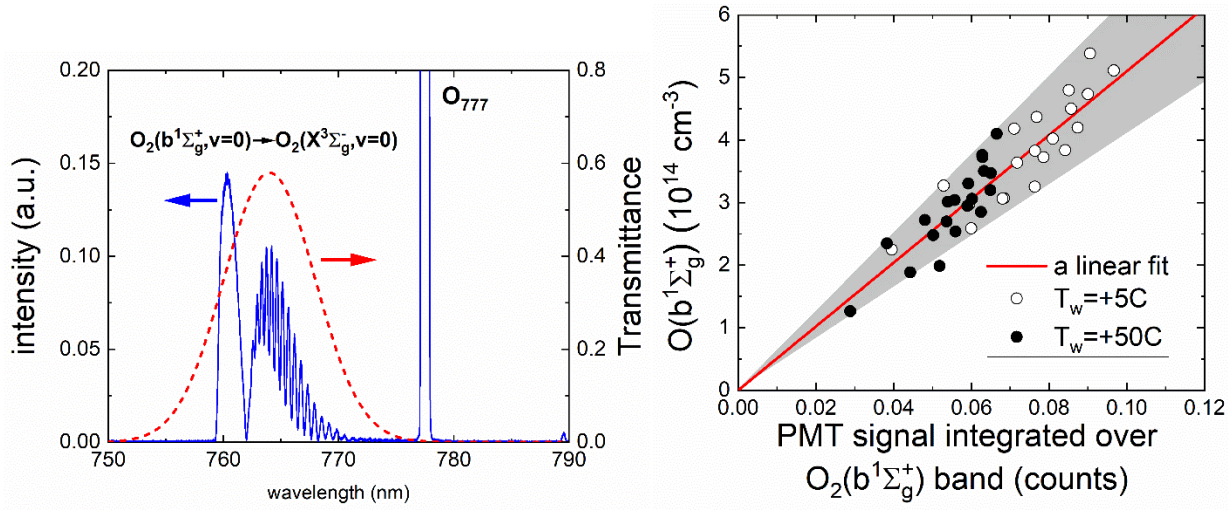

a) b)

Figure 3. a) Emission spectrum over the $O_2(b^1\Sigma_g^+)$ spectral region of an O_2 dc discharge at 1 Torr, 20 mA and T_w=+50C. The dashed line is the transmission curve of the interference filter used for absolute calibration of the $O_2(b^1\Sigma_g^+)$ concentration. b) Calibration plot for $O_2(b^1\Sigma_g^+)$ A-band integral (PMT signal integrated over the band) on $O_2(b^1\Sigma_g^+)$ density (for area close to the axis) estimated from the absolute emission measurements for pressures above 1 Torr. The red line is a linear fit of the data.

The Si detector was located at a distance of L ≈ 34 cm from the tube axis, and collected light from a 3 cm long axial section of the tube (selected using a rectangular mask). At this distance the selected section of the tube can be considered to approximate a "point" radiation source. The radiation power of this source is related to the number of $O_2(b^1\Sigma_g^+)$ molecules in the selected volume of the tube, i.e. the concentration, $\overline{[O_2(b^1\Sigma_g^+)]}$, averaged over the radial profile:

$$\overline{[O_2(b^1\Sigma_g^+)]} = \frac{4\pi L^2}{S_{\text{det}} \cdot \chi_{O2(b)}^{\text{IF}} \cdot \eta_{\text{det}}} \cdot \frac{1}{h\nu \cdot A \cdot V} \cdot I_{\text{det}} = C_{\text{cal}} \cdot I_{\text{det}} \qquad (1)$$

where C_{cal} is calibration coefficient, I_{det} is photodiode current, η_{det} is current/watt sensitivity (0.34 A/W) of the detector at 764 nm, $\chi_{O2(b)}^{\text{IF}}$ is the convolution of the filter transmittance with the A-band spectrum (it takes into account the distortion of the A-band spectrum by the filter transmittance), $h\nu$ is photon energy, A is the Einstein coefficient and $V=\pi R^2 \cdot x$ volume of the

selected are of the tube. Thus, knowing the average concentration and radial profile of $O_2(b^1\Sigma_g^+)$, it was possible to calibrate the density of $O_2(b^1\Sigma_g^+)$ molecules for all experimental conditions.

At pressures below 0.5 Torr, the emission from oxygen atoms increases strongly compared to the $O_2(b^1\Sigma_g^+)$ emission, both due to the lower $O_2(b^1\Sigma_g^+)$ density and to the strong increase in the excitation rate of atoms for higher reduced electric field, E/N. This leads to the appearance of an oxygen atom line (at 770.675nm) inside the A-band emission, as well as a significant increase in the intensity of the O_{777} line in comparison with the A-band. For this reason, the absolute calibration of the A-band intensity was only performed for pressures above 1 Torr, where oxygen atom emission can be neglected. Figure 3b compares the absolute $O_2(b^1\Sigma_g^+)$ density (determined from the absolutely-calibrated photodiode) to the integrated spectrum measured with the spectrometer photomultiplier. It can be seen that the relative accuracy of the calibration of the spectrometer sensitivity is ~20-25%. Spectral scans over a wider wavelength range showed mostly O atom lines, dominated by the intense well-known O_{777} and O_{844} lines. To confirm the absolute $O_2(b^1\Sigma_g^+)$ density we also performed vacuum ultraviolet absorption spectroscopy, described in the following section.

2.4. Measurement of $O_2(b^1\Sigma_g^+)$ density by VUV absorption

Western et al. [30] studied the VUV absorption spectra of $O_2(b^1\Sigma_g^+)$ molecules in a similar DC discharge, using the Fourier-transform Spectrometer at the DESIRS Beamline of Synchrotron Soleil. The rotational structure of several bands was analyzed, and *ab-initio* transition moments were calculated for all observed transitions in the VUV region. Western et al. calculated the absorption cross sections, and proposed a method to determine the absolute density of $O_2(b^1\Sigma_g^+)$ molecules using the (1-0) band of the $4p\pi^1\Sigma^+_u \leftarrow b^1\Sigma^+_g$ transition around 131.3nm. Optical emission measurements were carried out simultaneously with $O_2(b^1\Sigma_g^+)$ VUV absorption (data taken at the same time as for the article [30], allowing direct comparison of two techniques, as shown in figure 4. The $O_2(b^1\Sigma_g^+)$ density values obtained by OES were systematically higher than those from VUV absorption spectroscopy by a factor of about 1.5. This result is not surprising as the absolute calibration by absolute emission intensity measurements are subject to some uncertainty due to the difficulty of properly assessing the light collection efficiency. Therefore, considering the good agreement between the measured and ab initio VUV spectra, the OES measurements of $O_2(b^1\Sigma_g^+)$ were normalized to the VUV spectroscopy data.

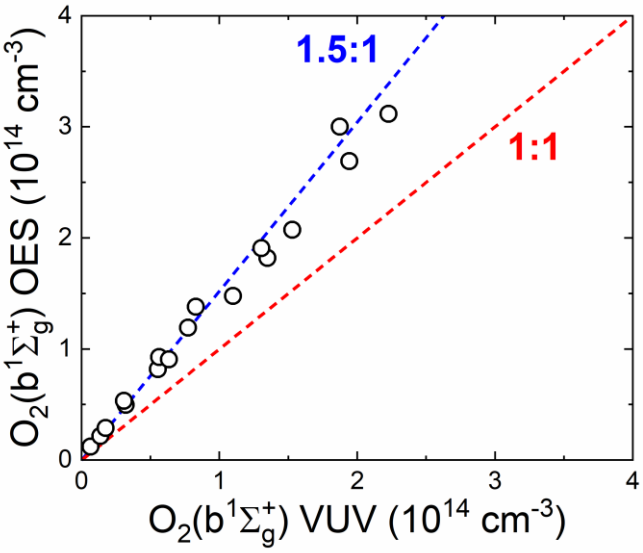

Figure 4. The comparison of $O_2(b^1\Sigma_g^+)$ concentrations at the tube axis obtained from the absolutely calibrated OES and VUV absorption at T_w=+50C.

2.5 Time-resolved sub-Doppler CRDS of O(^{3}P)

The density of O(^{3}P) atoms was determined using sub-Doppler CRDS of the forbidden O($^3P_2$) → O($^1D_2$) transition around 630nm, using a scheme similar to that presented by Peverall et al.[31]. Time-resolved measurements in modulated discharges were also made, by recording the phase of each CRDS event relative to the current modulation, and sorting the measurements into time-bins [27]. The setup is shown in figure 1. Spherical (1-metre radius) high-reflectivity mirrors (R ~ 0.9999 at ~630 nm) were installed at the ends of the tube, which provided a characteristic ring-down time of radiation in the empty cavity ($L_{cavity} \approx 75$ cm) of ~24 μs when the mirrors are new, but quickly degrading to the region of 5-10 μs. Tunable light in the vicinity of the transition at 630.205 nm was generated using an external-cavity cw diode laser (Toptica DL100) The laser beam is passed through an opto-acoustic modulator (AOM), and the first order scattered beam is injected into an optical fiber. The output from the fiber is collimated and focused into the CRDS cavity through the entrance mirror. The light escaping the exit mirror is detected by a photomultiplier (Hamamatsu R928) behind a 630 nm interference filter. The data acquisition and experiment control is managed by a Labview program through a National Instruments USB 6356 interface. The photomultiplier signal is digitized by an analog-to-digital converter in the USB 6356. Since the spectral width of the laser line is narrow compared to the spacing of the longitudinal modes of the cavity, the cavity length is scanned repetitively (at 30 Hz) by a piezo activator attached to the input mirror. When the cavity length is such that a longitudinal mode matches the laser wavelength, light intensity builds up in the cavity, and the output light intensity (detected by the photomultiplier) increases. When the detected signal passes a selected threshold, the AOM is shut off, and the cavity decay is recorded. The first 2 μs are typically rejected, to allow time for the AOM to shut off completely. The cavity decay time, τ, for each event is determined by fitting an exponential function using the Levenberg-Marquardt algorithm. The linear absorption coefficient of the medium inside the cavity is then determined from:

$$\alpha = \frac{L_{cavity}}{l_{O(3P)}} \cdot \frac{1}{c} \cdot \left(\frac{1}{\tau} - \frac{1}{\tau_0}\right) \quad (2)$$

where α - absorption in cm^{-1}, c - speed of light, τ - characteristic cavity time (with discharge), τ_0 - characteristic cavity time (without discharge), L_{cavity} - cavity length, $l_{O(3P)}$- tube length between metal inserts, where oxygen atoms are present (in fact, this is the length of the positive discharge column along the laser beam).

The Doppler profile is typically scanned over about 3 minutes to achieve adequate signal-to-noise ratio. Examples of measured O($^3P_2$) → O($^1D_2$) absorption line profiles for different pressures are shown in figure 5.

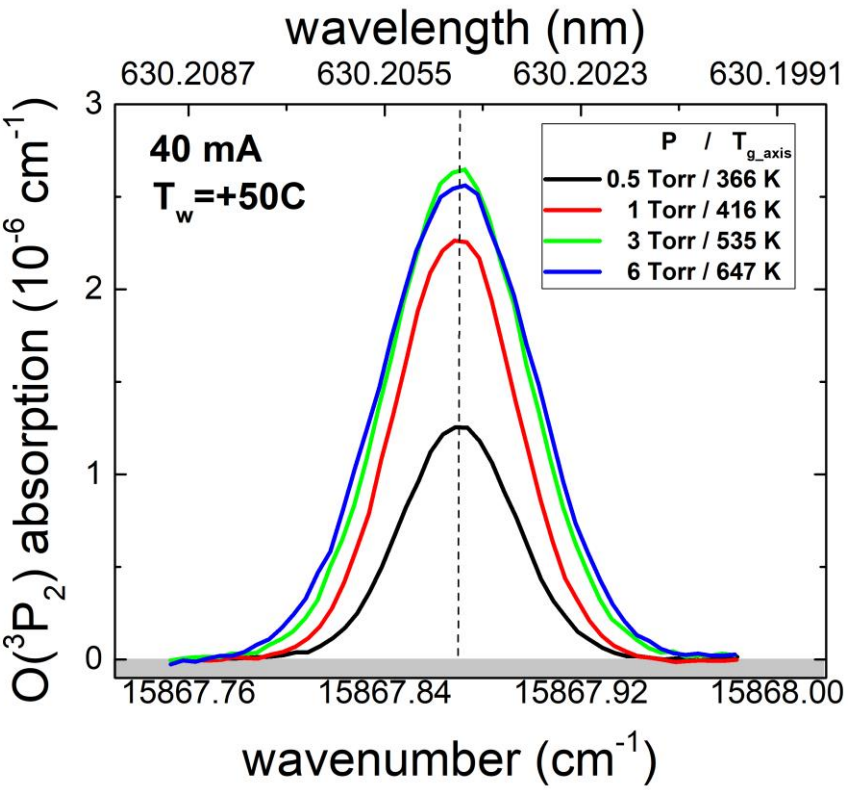

Figure 5. Examples of measured absorption line profiles at the $O(^3P_2) \rightarrow O(^1D_2)$ transition for pressures of 0.5, 1, 3, 6 Torr and current of 40 mA. The atom temperatures obtained from fitting the profiles by the Doppler profile are presented in the legend.

The atom temperatures obtained from fitting the profiles by a Doppler profile are presented in the legend. The temperature determination accuracy was better than ~ 5%. The integrated absorption cross section for the $O(^3P_2) \rightarrow O(^1D_2)$ transition is $\sigma_{int} = 2.98 \cdot 10^{-23}$ cm^2/cm^{-1}:

$$\sigma_{\text{int}} = \int \sigma_{\text{low}}^{\text{up}} d\nu = \frac{g_{\text{up}}}{g_{\text{low}}} \frac{A_{\text{low}}^{\text{up}} \lambda^2}{8\pi} \tag{3}$$

where A_{low}^{up} is the Einstein coefficient for the $O(^3P_2) \rightarrow O(^1D_2)$ transition, g_{up} is the degeneracy degree for the upper $^1D_2$ state (g_{up} = 5), g_{low} is the degeneracy degree for the lower $^3P_2$ state (g_{low} = 5), g_J = 5, 3 and 1 for J = 2, 1 and 0 respectively. The populations of the $O(^3P_J)$ states are close to equilibrium with the gas translational temperature[31] . The total number density of $O(^3P)$ atoms was then calculated from $O(^3P_2)$ density using the relation:

$$[O(^3P)] = \frac{\sum_J g_J e^{-E_J/\text{kT}} [O(^3P_2)]}{g_2} \tag{4}$$

A software algorithm was developed to sort the "CRDS events" in time (and, accordingly, the observed absorption) relative to the phase of the current modulation, which made it possible to implement the time-resolved sub-Doppler CRDS method and thereby observe the dynamics of $O(^3P)$ atoms during discharge modulation.

3. Model description

A one-dimensional 1D(r) self-consistent discharge and chemical kinetic model was developed to simulate a DC oxygen discharge in a tube, using the local electric field approximation for the

electron energy distribution function. The standard continuity equations are used to calculate the spatial distributions of all charged and neutral gas species in the radial direction:

$$\frac{\partial n_i(r,t)}{\partial r} = \frac{1}{r}\frac{\partial}{\partial r}\left(r\left(D_i N \frac{\partial X_i}{\partial r}\right) - q_i \mu_i E_r n_i\right) + S_i(r,t) \quad (5),$$

where N is the total gas number density, n_i and X_i are the concentration and mole fraction of a species indexed by "i", D_i and μ_i are diffusion and mobility coefficients of corresponding specie and S_i is the total rate of production-loss of a specie in different reactions, E_r – is the radial electric field, calculated from the Poison equation:

$$\frac{1}{r}\frac{\partial}{\partial r} r E_r = -4\pi \sum_i q_i n_i \quad (6),$$

where q_i - is a charge of the corresponding particle. The pressure and temperature dependences of the diffusion coefficients for neutral and ionic components were assumed to be: $D_i \propto T^{3/2}/P$ and $D_+ \propto T^2/P$ following [32]. The electron energy distribution function (EEDF) is determined as a function of the local reduced electric field by solving Boltzmann equation in the two-term approximation (including the effect of inelastic and superelastic collisions with excited states of oxygen molecules and atoms). The electron transport coefficients (D_e and μ_e, the drift velocity) and the rate constants for reactions involving electrons are then calculated from the EEDF.

The longitudinal component of the electric field, E_z, was assumed to be constant across the radius, r. This allows the electron density to be deduced from the experimental value of the total current through the drift velocity, determined as a function of the reduced electric field.

The boundary conditions for equations (5) and (6) include the symmetry condition on the tube axis (r = 0) and the losses of the species on the tube wall (at r = R, the tube radius), which occur with probabilities γ_i.

The model also takes into account the heating of the gas in the discharge. The gas temperature T(r,t) (assuming constant gas pressure) was found from the simultaneous solution of the equations for the total enthalpy of the mixture - H(r,t):

$$\frac{\partial H(r,t)}{\partial r} = J_z E_z + \frac{1}{r}\frac{\partial}{\partial r}\left(r\lambda \frac{\partial T}{\partial r}\right) + \sum_i h_i J_{D_i} \quad (7),$$

$$H(r,t) = \sum_i h_i n_i = \sum_i n_i \left(\int_0^T C_{P_i}(T)\, dT + h_{0_i}\right) \quad (8)$$

These equations were solved considering the following terms: Joule heating - $J_z E_z$ (J_z is the current density in the axial direction, E_z is the longitudinal electric field), the gas thermal conductivity (assumed to be $\lambda = 33 \cdot T^{0.78}$ erg/(s·cm·K), based on the experimental data from [33]), a heat flux $J_{Di} = - D_i/N \cdot \nabla \cdot (n_i/N)$ for each i-th component of the mixture. In equation (8), C_{pi} and h_{0i} designate the heat capacity and the enthalpy of formation of the i-th component of the mixture, correspondingly. The heat capacities of each component, $C_{pi}(T)$, were expressed as polynomial functions: $C_{P_i}(T) = \sum a_{ij} T^j, j = 0 - 4$, where a_{ij} were taken from Burcat and Ruscic [34]. The wall temperature was set to 323K, as in the experiment. The total particle concentration N as a function of the gas temperature T was determined from the ideal gas equation at constant pressure.

The equations (5)-(8) are solved for the steady-state discharge and afterglow, using a numerical method specially developed for stiff systems of differential equations. The EEDF is recalculated as necessary to account changes in the local gas composition.

The time-dependent equations for the particle number densities, the EEDF(r,t), the gas temperature T(r,t), and the axial electric field $E_z(t)$ are solved self-consistently until steady-state is reached, setting the current as the input parameter.

The modulated discharge is simulated in the following way. First, the stationary discharge is calculated for a current value corresponding to the experimental current before the fast current decrease. Then the experimental current as a function of time is used as input parameter for the modulation phase simulation. In this approach, the exact experimental discharge current behavior is simulated with time. This is important at high gas pressure values, when current change during modulation differs from the ideal step function.

3.1 Reaction scheme

The reaction scheme for heavy particle kinetics and electron scattering on excited molecules are based on the work of Braginsky et al.[24], Kovalev et al.[35], Vasilieva et al.[36] and Ivanov et al. [37]. The cross-section set for electron scattering on ground state $O_2(X^3\Sigma_g^-)$ molecules is taken from Lawton and Phelps[38]. The model includes all major charged and neutral particles: electrons, negative ions (O^-, O_2^- and O_3^-), positive ions (O^+, O_2^+ and O_4^+), vibrationally excited $O_2(v)$ molecules (v up to 40), metastable molecules ($O_2(a^1\Delta_g)$, $O_2(b^1\Sigma_g^+)$ and O_2^{**} (an effective sum of the $O_2(A'^3\Delta_u$, $A^3\Sigma_u^+$, $c^1\Sigma_u^-$, Hertzberg states), $O(^3P)$, $O(^1D)$, $O(^1S)$ atoms and O_3 molecules and a detailed plasma-chemical reaction scheme for all these components.

The main production reactions for $O_2(b^1\Sigma_g^+)$ are reactions (R1)-(R3) in Table 1a under our discharge conditions, the most important of which is energy transfer from $O(^1D)$ (reaction (R1)). The quenching of $O(^1D)$ by ground-state $O_2(X^3\Sigma_g^-)$ has been experimentally studied by many groups [39-45]. There are three possible channels for this reaction:

$$O(^1D) + O_2(X^3\Sigma_g^-) \rightarrow O_2(b^1\Sigma_g^+) + O(^3P) \quad \text{(R1a)}$$
$$\rightarrow O_2(X^3\Sigma_g^-, v) + O(^3P) \quad \text{(R1b)}$$
$$\rightarrow O_2(a^1\Delta_g) + O(^3P) \quad \text{(R1c)}$$

The mechanism and pathways were investigated by Miura and Hashimoto [46] and Grebenshchikov et al. [47] using quantum-mechanical calculations. They concluded that the dominant pathway is a pseudo-crossing with $O + O_2(b^1\Sigma_g^+)$ at large $O–O_2$ separation. It was shown [48] that the other pathways are possible also. However, these pathways either involve the successive nonadiabatic transitions or realized via the higher-energy pseudocrossings. Therefore, probabilities of these transitions are low. The branching ratios have been also determined experimentally. Lee and Slanger [41] made time-resolved measurements of the $O_2(b^1\Sigma_g^+,v)$ and $O(^1D)$ emissions, and found that $O_2(b^1\Sigma_g^+)$ is produced with an efficiency of ~ (0.77±0.23). In their experiment, $O(^1D)$ atoms were produced from O_2 photo-dissociation (using an H_2 laser at ~160 nm) and were detected by the $O(^1D) \rightarrow O(^3P)$ emission at 630 nm. Pejakovic et al. [48] found that $O_2(b^1\Sigma_g^+)$ is produced only in the v=1 vibrational level. Gauthier and Snelling [49] reported that the efficiency of $O_2(a^1\Delta_g)$ production is less than 0.05. Snelling [50] found that the production of $O_2(X)$ was two orders smaller than the total quenching rate, although McCullough et al.[51] reported an efficiency as high as 0.3-0.4 for the vibrational levels v=13-15. The temperature dependence of the total rate constant for R1 is based on the measurements between 104 - 354 K by Streit et al. [39] and over the 50-209 K region by Grondin et al. [45]. Close values of the (R1) rate constant in this temperature range were also obtained by Dunlea et al. [52] and Strekowski et al. [53]. These measurements all show that the rate constant in this temperature range has slight negative temperature dependence, which is consistent with the formation of an intermediate complex.

To the best of our knowledge, there are no reliable experimental or theoretical data on rate constant and reaction pathways of (R1) at higher temperatures. Blitz et al. [54] studied the $O(^1D)$ loss rate in collisions with various gases (including O_2) over the temperature range 195–673 K, using either vacuum ultraviolet laser induced fluorescence (VUV LIF) detection of $O(^1D)$ at 115.2,

or LIF detection of OH generated from the reaction of $O(^1D)$ with H atom donor species as a marker for $O(^1D)$ atoms. This study gave higher rate constants in the low temperature range (50-354 K), but showed a steeper decrease in rate with temperature (exp(87/T)). However, this study did not distinguish between the reaction products. Therefore, we have assumed that reaction (R1) produces $O_2(b^1\Sigma_g^+,v=1)$ with an efficiency of 0.8 from total $O(^1D)$ quenching on O_2 molecules followed by fast intermolecular relaxation to $O_2(b^1\Sigma_g^+,v=0)$ [55]. We used the temperature dependence of the reaction constant obtained by Streit [39] and recommended by Atkinson et al. [56].

For the creation of $O_2(b^1\Sigma_g^+)$ by electron impact on the ground state (process R2 in table 1a) the cross section from Lawton and Phelps [38] is used. Recent experimental data [57] and R-matrix quantum mechanical calculations [58] of the cross section show a resonance peak at an electron energy of 8 eV. However, for the values of the reduced electric field in this study the rate constants calculated with these two cross sections are quite similar. A slight difference for the reduced electric fields higher than 100 Td is not significant for this work.

For the creation of $O_2(b^1\Sigma_g^+)$ by electron impact on $O_2(a^1\Delta_g)$, (R3), we use a cross section with the same shape as for excitation from the ground state, but with a corresponding shift in the energy threshold [37], and increased in magnitude to match the value measured by Halle et al. [59] at 4.5 eV. Recent the R-matrix quantum calculations [58] of the cross section for (R3) process lead to similar values of the rate constant for (R3).

Table 1a. Principal reactions producing $O_2(b^1\Sigma_g^+)$.

№	Reaction	Rate constant, cm^3/s	Reference
(R1)	$O(^1D) + O_2(X^3\Sigma_g^-) \rightarrow O_2(b^1\Sigma_g^+)+O(^3P)$ (a) $\rightarrow O_2(X^3\Sigma_g^-,v)+ O(^3P)$ (b) $\rightarrow O_2(a^1\Delta_g) + O(^3P)$ (c)	$2.56\cdot10^{-11}\cdot\exp(67/T)$	[39]
(R2)	$e + O_2(X^3\Sigma_g^-) \leftrightarrow e + O_2(b^1\Sigma_g^+)$	EEDF	[38]
(R3)	$e + O_2(a^1\Delta_g) \leftrightarrow e + O_2(b^1\Sigma_g^+)$	EEDF	[58]

As the main production channel of $O_2(b^1\Sigma_g^+)$ is the energy transfer from $O(^1D)$ atoms, it is necessary to briefly discuss reactions involving $O(^1D)$ and $O(^3P)$, shown in Table 1b. For the electron-impact excitation of $O(^3P)$ atoms to the $O(^1D)$ state (R9) the cross section set from the Laher et al. [60] is used. Recent calculations by Zatsarinny and Tayal [61] using the B-spline R-matrix approach give a similar cross section for this process. For the dissociation of O_2 molecules in Schumann-Runge continuum (R8) the cross section from the Phelps cross section set [38] is used. A more detailed analysis of the dissociation processes will be discussed in a separate paper.

For the reaction (R10) a rate constant of $8\cdot10^{-12}$ cm^3/s was used, obtained by Yee et al. [62] where the multi-state diabatic formulation was used to calculate the collision-induced quenching of $O(^1D)$. The calculated rate constant is in agreement with the empirical atmosphere data of Abreu et al. [63]. Also, for completeness of the kinetic scheme, the reaction (R11) of quenching $O(^1D)$ by $O_2(a^1\Delta_g)$ with the rate constant proposed by Doroshenko et al. [64] is included.

Table 1b. Principal reactions for $O(^3P)$ and $O(^1D)$.

№	Reaction	Rate constant, cm^3/s	Reference

(R8)	$e + O_2(X^3\Sigma_g^-) \rightarrow e + O(^3P) + O(^1D)$	EEDF	[38]
(R9)	$e + O(^3P) \rightarrow e + O(^1D)$	EEDF	[60]
(R10)	$O(^1D) + O(^3P) \rightarrow O(^3P) + O(^3P)$	$8 \cdot 10^{-12}$	[62], [63]
(R11)	$O(^1D) + O_2(a^1\Delta_g) \rightarrow O(^3P) + O_2(X^3\Sigma_g^-, v)$	$1 \cdot 10^{-11}$	[64]
(R13)	O atom wall loss	see text	[28]

The most important known reactions for $O_2(b^1\Sigma_g^+)$ loss (prior to this work) are shown in table 1c. The quenching of $O_2(b^1\Sigma_g^+)$ by O_2 molecules has been studied by Borell et al.[65], who measured the temperature dependence of the rate constant in a shock tube experiment in the 295 - 1800 K temperature created by pulsed tunable dye laser pumping from the O_2 ground state, and used the time-resolved emission from the $O_2(b^1\Sigma_g$ v = 0) - $O_2(X^3\Sigma$, v=0) transition to measure the rate constants of $O_2(b^1\Sigma_g^+)$ quenching by O_2 in the 297 - 800 K temperature range. They found a rate described by $k_{O2} = (7.4 \pm 0.8) \cdot 10^{-17} \cdot T^{0.5} \cdot \exp(-(1104.7 \pm 53.3)/T)$ cm^3/s, with an activation energy of 95meV. It should be noted that the shock tube experiment of Borell et al [65] overestimates the rate constant at room temperature. Therefore, in this work, we used data from Zagidullin et al.[66]. However, despite the increased gas temperatures observed in our experiments at higher pressures and currents, the rate of this is insignificant compared to the rates of surface loss of $O_2(b^1\Sigma_g^+)$.

Table 1c. Principal loss reactions for $O_2(b^1\Sigma_g^+)$.

№	Reaction	Rate constant, cm^3/s	Ref.
(R4a)	$O_2(b^1\Sigma_g^+) + O_2 \rightarrow 2O_2(X^3\Sigma_g^-)$	$(7.4 \pm 0.8) \cdot 10^{-17} \cdot T^{0.5} \cdot \cdot \exp(-(1104.7 \pm 53.3)/T)$	[65],[66]
(R4)	$O_2(b^1\Sigma_g^+) + O(^3P) \rightarrow O_2(a^1\Delta_g) + O(^3P)$ (a) $\rightarrow O_2(X^3\Sigma_g^-) + O(^3P)$ (b)	$8 \cdot 10^{-14}$	[40]
(R5)	$O_2(b^1\Sigma_g^+) + O(^3P) \rightarrow O(^3P) + O_2(X^3\Sigma_g^-)$	$k_5 \cdot \exp(-T_5/T)$	this work
(R6)	$O_2(b^1\Sigma_g^+) + O(^3P) \rightarrow O(^1D) + O_2(X^3\Sigma_g^-)$	$3.39 \cdot 10^{-11} \cdot (300/T)^{0.1} \cdot \cdot \exp(-4201/T)$	[67]
(R7)	$O_2(b^1\Sigma_g^+) + O_3 \rightarrow O_2(X^3\Sigma_g^-) +$ $+ O_2(X^3\Sigma_g^-, v=3) + O(^3P)$	$1.5 \cdot 10^{-11}$	[40]
(R12)	$O_2(b^1\Sigma_g^+)$ quenching at the glass walls	$\gamma = 0.135$	this work

Reactions (R4) - (R7) are the most significant volume loss reactions for $O_2(b^1\Sigma_g^+)$. Quenching at the wall (R12) dominates at lower gas pressure due to the large surface loss probability coefficient, γ_{O2b} = 0.135. The effective loss frequency for the given species (for example $O_2(b^1\Sigma_g^+)$, or O atoms) due to destruction at a wall surface (by quenching or recombination, for example) is related to the surface loss probability, γ, by:

$$\nu_{wall} = \gamma \cdot \frac{N_{nw}}{<N>} \cdot \frac{v_{th}}{4} \cdot \frac{2}{R} \ , \qquad (9)$$

Where N_{nw} is the species density near the wall, $<N>$ is the radially average density (with $N_{nw}/<N> \approx 1$ at low pressure or for small γ), v_{th} is the thermal velocity, and $2/R$ - is the S/V ratio in the cylindrical geometry.

The rate of collisional quenching of $O_2(b^1\Sigma_g^+)$ by O atoms at room temperature, (R4) was studied by Slanger et al. [40], who measured a rate constant of $(8\pm2)\cdot10^{-14}$ cm^3/s. The recommended branching ratio for the production of $O_2(a^1\Delta_g)$ through this reaction is ~0.75 [56]. In this work, we used a rate constant $k4 = 8 \cdot 10^{-14}$ cm^3/s with a channel efficiency (R4a) equal to 0.875. The effect of varying the rate constant over the recommended range was also considered.

The rate of quenching of $O_2(b^1\Sigma_g^+)$ to produce $O(^1D)$ atoms ((R6), the reverse of process (R1)) was calculated from thermodynamic equilibrium constant and rate constant of the forward reaction by Zinn [67]. The rate of $O_2(b^1\Sigma_g^+)$ quenching by ozone (R7) was measured by Slanger et al. [40].

As will be discussed in section 5, the existing model was unable to fit the observed results without the addition of a thermally-activated reactive quenching process for the destruction of $O_2(b^1\Sigma_g^+)$ by collision with O (^3P) atoms, (R5). The temperature dependent quenching reaction (R5) will be referred to hereinafter as the "reactive quenching" processes to distinguish it from reaction (R4). However, at this time we cannot say for certain that the process (R5) is due to a reactive mechanism only. To prove this pathway of the quenching reaction (R5), experiments with isotopes are needed, as was done for the reactions of ozone formation [68]. The coefficients for this reaction rate were optimized to fit the experimental data, which will be discussed in section 5.

4. Experimental results

The observed variation of the average density of $O_2(b^1\Sigma_g^+)$ as a function of pressure for different currents is shown in figure 6. At 20 mA the $O_2(b^1\Sigma_g^+)$ density passes through a maximum with pressure at about 5 Torr (it was not possible to sustain the discharge at 10mA above 2 Torr). For higher discharge currents the same behavior is observed, but the maximum shifts to lower pressure. Interestingly, whereas below these maxima the $O_2(b^1\Sigma_g^+)$ density increases with discharge current, above the maxima this trend is reversed. This surprising result indicates that there is a significant $O_2(b^1\Sigma_g^+)$ loss process which increases with pressure and current more quickly than the rate of production of $O_2(b^1\Sigma_g^+)$ (which would be expected to increase with both the ground state $O_2(X^3\Sigma_g^-)$ density and the electron density. In order to explain these observations, we will now look at the ground-state oxygen atom densities and the gas temperature determined by CRDS. Figure 7 shows the $O(^3P)$ density (from CRDS) and gas temperature as a function of pressure at different currents. The oxygen atom density increases with gas pressure and discharge current, as does the gas temperature. The observed trends in the $O_2(b^1\Sigma_g^+)$ density with pressure and current can therefore be explained by the onset of a quenching reaction of $O_2(b^1\Sigma_g^+)$ by O ^3P atoms with a significant activation energy. Such a process will be negligible at low pressure and current (when both the oxygen atom density and the gas temperature are low), but will become dominant at high pressure and current.

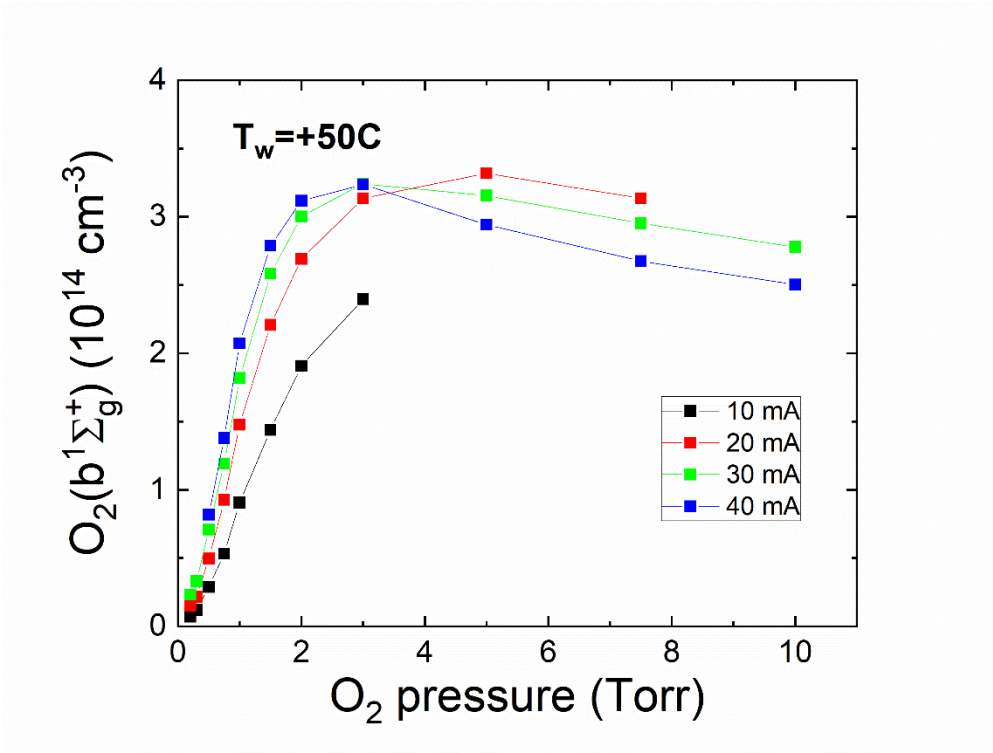

Figure 6. $O_2(b^1\Sigma_g^+)$ density as a function of pressure at different currents (experimental data).

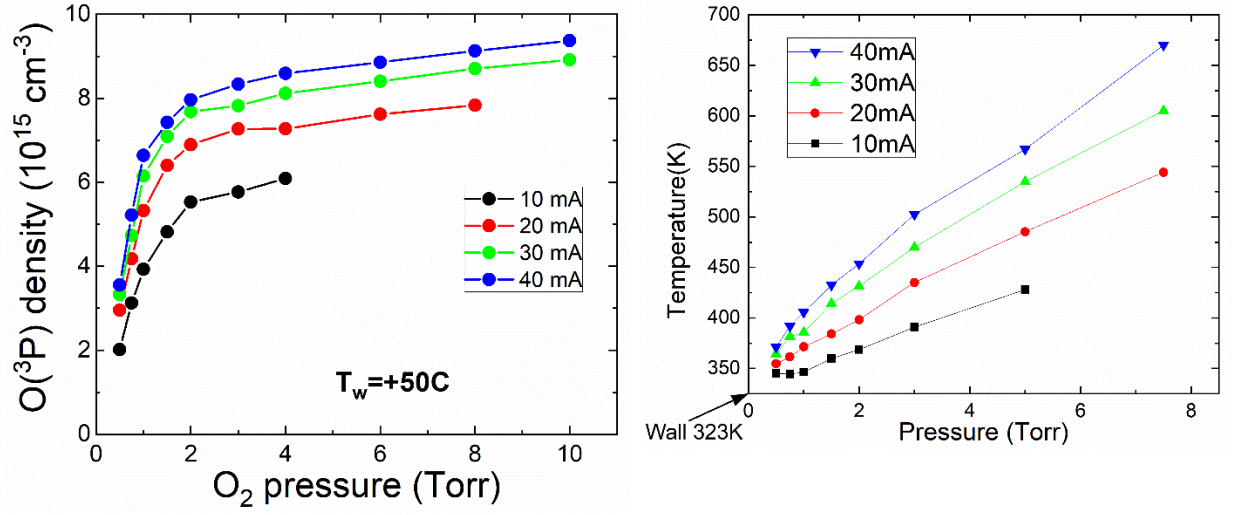

(a) (b)

Figure 7. $O(^3P)$ density (CRDS data) *(a)* and gas temperature *(b)* as a function of pressure and discharge currents (experimental data).

Further information can be obtained from the radial profiles of the $O_2(b^1\Sigma_g^+)$ density, examples of which are presented in figure 8. For a current of 30mA. The tube walls and the window boundaries at the ends of the tube are shown by a grey area. The $O_2(b^1\Sigma_g^+)$ measurement is truncated at the border of the near window, while the difference between the observed positions of the windows allows an estimation of the spatial resolution. In the ideal case of the parallel rays, one would see the same position of the two windows. To provide a long depth of focus (depth resolution) along the tube and correspond to the ideal case, one would need to move the spectrometer very far from the tube. But in this case, the spatial resolution in the radial direction will be worse. An optimal

distance between the spectrometer and the tube provides reasonable resolution in the radial direction with the reasonable image blur in the axial direction (due to the small depth of focus). In this case, the image of the nearest tube window at the spectrometer entrance will be partly diffusive (since it is out of the focus) and a slightly bigger diameter than the image of the far tube window. In this sense, the difference between the seen positions of the windows can be considered a parameter determining the spatial resolution - about 0.09 cm in our case.

The radial $O_2(b^1\Sigma_g^+)$ profile is quite diffuse, with a maximum at the tube axis, even at the lowest pressure (< 0.5 Torr), where the rate of $O_2(b^1\Sigma_g^+)$ volume loss is small and the $O_2(b^1\Sigma_g^+)$ diffusion frequency is relatively high $\nu_{DO2} > 3000\ s^{-1}$. This indicates that the loss probability of the $O_2(b^1\Sigma_g^+)$ on the borosilicate glass surface is rather high, of the order, $\gamma_{O2b} > 0.1$. The effective surface quenching frequency of $O_2(b^1\Sigma_g^+)$ will decrease with increasing pressure. However, with increasing pressure, the radial profile of $O_2(b^1\Sigma_g^+)$ becomes flatter, indicating the onset of a volume quenching process at higher pressure. In order to affect on the profile, the rate of this volume process must be comparable to that of the surface process. None of the currently-known $O_2(b^1\Sigma_g^+)$ volume quenching processes, involving either O_2 molecules or $O(^3P)$ atoms, can explain such a high quenching rate. It should also be noted that the concentration of O_3 is far too low under these conditions to affect the quenching of $O_2(b^1\Sigma_g^+)$. Therefore, the observed change in the $O_2(b^1\Sigma_g^+)$ radial density profile of with pressure can only be explained by the onset of a new quenching process at high pressure.

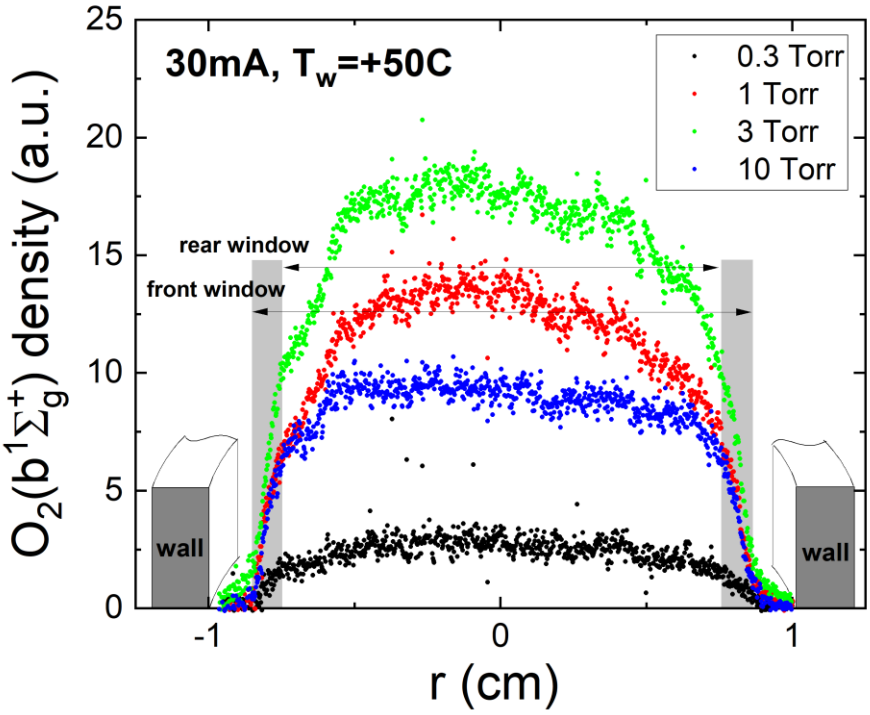

Figure 8. Examples of the radial profiles of $O_2(b^1\Sigma_g^+)$ for 30 mA and pressure 0.5, 1, 3 and 10 Torr. The observed profiles are limited by the window size (~16mm), which was less than the tube diameter (20mm).

To verify this, kinetic experiments were performed during partial modulation (15%) of the discharge current. We observed the temporal response of the $O_2(b^1\Sigma_g^+)$ density (optical emission), the $O(^3P_2)$ density (CRDS) and the oxygen mole-fraction (actinometry measurements. Two current modulation sequences were used – "fast" (5 ms high current and 6ms low current) and "slow" (200ms high and low current).

Figure 9 shows the $O_2(b^1\Sigma_g^+)$ dynamics during fast modulation. The discharge current is switched between high and low current modes within a few μs. At 1 Torr (figure 9a) the $O_2(b^1\Sigma_g^+)$ density increases when the discharge current is increased, and decreases when the discharge current is decreased. The $O_2(b^1\Sigma_g^+)$ density does not respond instantaneously to the current change, but with a relaxation time of about 1 ms which can be attributed to the $O_2(b^1\Sigma_g^+)$ lifetime. At higher current this time constant becomes shorter.

With increasing pressure, the dynamics of $O_2(b^1\Sigma_g^+)$ becomes more complex. After the transition to lower current the $O_2(b^1\Sigma_g^+)$ density drops (as at lower pressure) with a sub-millisecond response time (and similarly increases as the current is stepped up). However, over a longer timescale, the $O_2(b^1\Sigma_g^+)$ density changes in the opposite direction. For example, at 3 and 8 Torr pressure (see figure 9b and c), when the discharge current is stepped up, the $O_2(b^1\Sigma_g^+)$ density first increases rapidly (in less than 1 ms) in response to the discharge current increase, reaches a maximum, then decreases with a longer characteristic time. After the current is stepped down, everything happens in the opposite order. This slow trend at higher pressure in the $O_2(b^1\Sigma_g^+)$ density with current is coherent with the trend in the steady-state density, which decreases with increasing current (see figures 9b, 9c and 6)

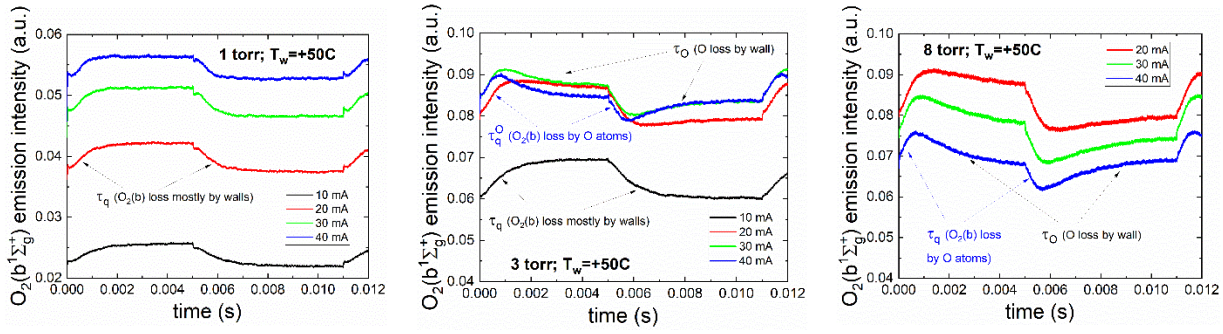

(a) (b) (c)

Figure 9. Examples of the $O_2(b^1\Sigma_g^+)$ density dynamics, during fast (5ms on/6ms off) partial modulation, at pressures of (a) 1, (b) 3 and (c) 8 Torr.

Figure 10 shows the dynamics of the $O_2(b^1\Sigma_g^+)$ density during the slow current modulation scheme. Two time constants are observed in this case: first a rapid response in the same direction as the current change, corresponding to processes observed during "fast" modulation conditions. This response represents changes in the $O_2(b^1\Sigma_g^+)$ production rate, due to the rapid changes of the electron density, reduced electric field and gas temperature. The second, slower, process occurs in the other direction, and is accompanied by only small changes of electric field and gas temperature. This slower timescale is comparable to that of the variation in the $O(^3P)$ density. On this slower time-scale, the $O_2(b^1\Sigma_g^+)$ density is in a quasi-steady-state, determined by the balance of production and loss processes; the production rate (determined principally by the electron density and the reduced electric field) is almost constant, but the loss rate changes due to the slowly-changing $O(^3P)$ which quenches $O_2(b^1\Sigma_g^+)$ at higher gas pressures and temperatures. At 1 Torr (see figure 10a), the steady-state concentration of $O_2(b^1\Sigma_g^+)$ follows the current modulation. In this case, the dominant $O_2(b^1\Sigma_g^+)$ loss process is quenching at the walls of the tube, and volume processes are negligible. At higher pressure and discharge current, the quasi-steady-state concentration of $O_2(b^1\Sigma_g^+)$ no longer follows the current. At 8 Torr the steady-state $O_2(b^1\Sigma_g^+)$ density decreases when the current increases, and reaches a steady state with the same characteristic time as the $O(^3P)$ density, i.e. it follows the dynamics of $O(^3P)$ atoms.

Figure 11 shows the dynamics of $O(^3P_2)$ atoms measured by time-resolved CRDS. Immediately after the current changes, fast jumps in the $O(^3P_2)$ density are observed, caused by

jumps in the gas temperature, causing jumps in the total gas density. The red lines in figures 11 show exponential fits to the growth and decay curves of [O($^3P_2$)], from which the loss frequencies of O atoms can be determined. Booth et al.[28], showed that oxygen atoms in a similar DC discharge are predominantly lost by recombination on the tube surface, and gave a detailed model of this process.

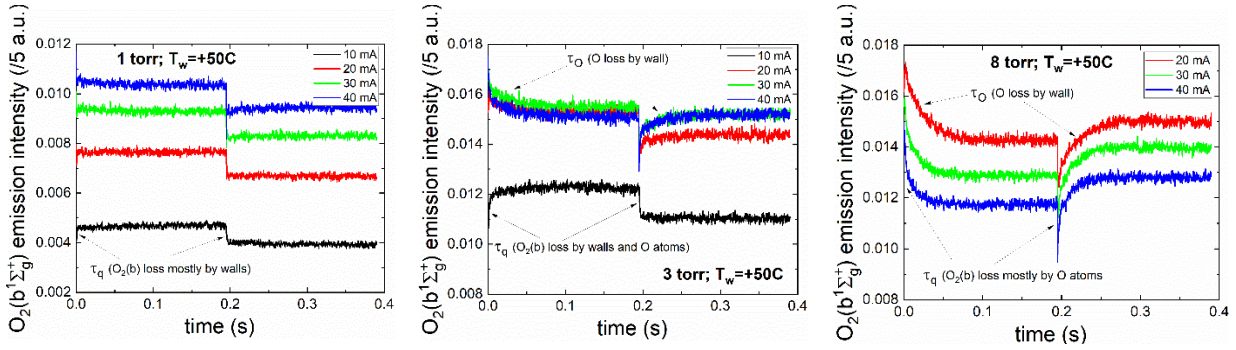

(a) (b) (c)

Figure 10. Examples of the $O_2(b^1\Sigma_g^+)$ density dynamics for pressure 1 (a), 3 (b) and 8 Torr (c) at the partial (~15%) "slow" modulation.

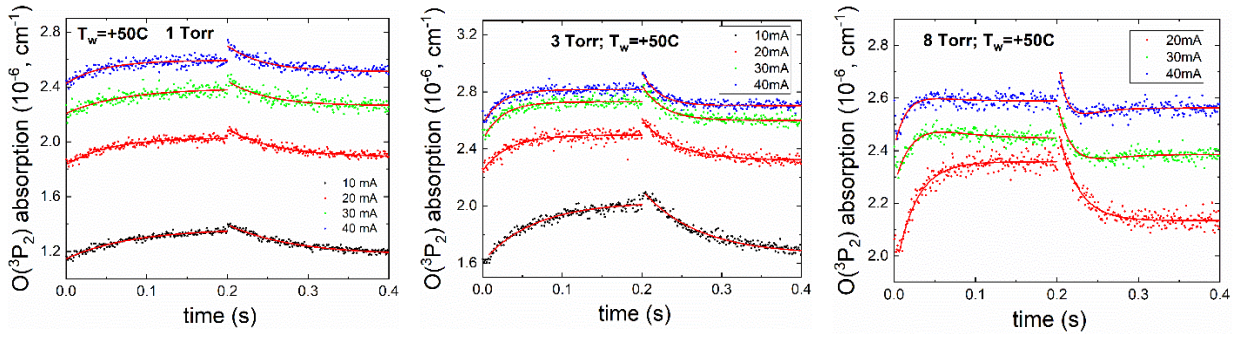

(a) (b) (c)

Figure 11. Examples of the O($^3P_2$) absorption dynamics (CRDS data) for pressure 1 (a), 3 (b) and 8 Torr (c) during "slow" modulation. Red lines are fits.

Comparing the dynamics of $O_2(b^1\Sigma_g^+)$ density with that of O(^{3}P) atoms shows that the change in the quasi-steady-state concentration of $O_2(b^1\Sigma_g^+)$ occurs with the characteristic loss frequency of oxygen atoms, but in antiphase. An increase in the O(^{3}P) concentration leads to a decrease in the $O_2(b^1\Sigma_g^+)$ concentration. The electron density and EEDF are changing with the same timescale as gas temperature, that is to say with a characteristic time of a few ms. Oxygen atoms react more slowly, on a time-scale determined by the loss rate at the walls. These different time scales allow us to identify the quenching process of $O_2(b^1\Sigma_g^+)$ by O(^{3}P) atoms and not some third specie affecting both densities. The tube wall also cannot be that third specie, because the wall loss coefficients for O(^{3}P) atoms and $O_2(b^1\Sigma_g^+)$ molecules differ by 2 orders of magnitude, so again the characteristic times are different. The higher the pressure and discharge current, the more significant the role of atoms in the quenching of $O_2(b^1\Sigma_g^+)$, and, as can be seen in figure 9, the higher the rate of $O_2(b^1\Sigma_g^+)$ quenching. Thus, the experimental results are fully consistent with the presence of a thermally-activated quenching process of $O_2(b^1\Sigma_g^+)$ molecules by oxygen atoms.

The experimentally observed $O_2(b^1\Sigma_g^+)$ loss frequencies, $\nu_{loss}^{O2(b)}$, are presented in figure 12 as a function of pressure at different currents. They were estimated from exponential fits of $O_2(b^1\Sigma_g^+)$ dynamics during "fast" modulation, taking into account also the slow drift of the quasi-

steady-state $O_2(b^1\Sigma_g^+)$ value due to variation in the $O(^3P)$ density. The "zero pressure" gray point, marked by the arrow, show the loss frequency value from which γ_{O2b} value was obtained.

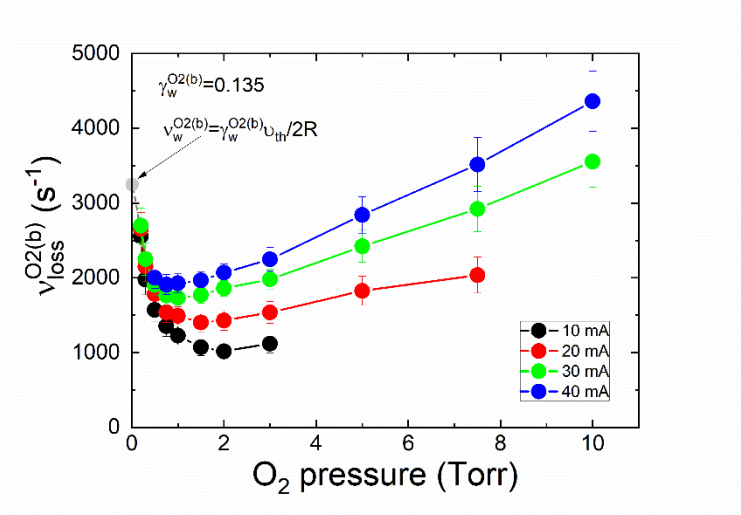

Figure 12. $O_2(b^1\Sigma_g^+)$ loss frequencies as a function of pressure at different current.

5. Model results and discussion

5.1 Gas temperature and $O(^3P)$ density

Before a detailed discussion on reactive quenching of $O_2(b^1\Sigma_g^+)$ by $O(^3P)$ atoms, we will demonstrate that the model correctly describes the primary experimental data related to the rate of the additional quenching: gas temperature and $O(^3P)$ atom density.

The calculated and measured gas temperature at the tube axis, T_{g_axis}, and the radially averaged value, T_{g_aver}, are shown in figure 13 by red and black lines correspondingly. It is seen that the model adequately describes both the axial value of gas temperature and radial profile of T_{gas}, as the model provides a good agreement between experimental and calculated radially averaged values, T_{g_aver}.

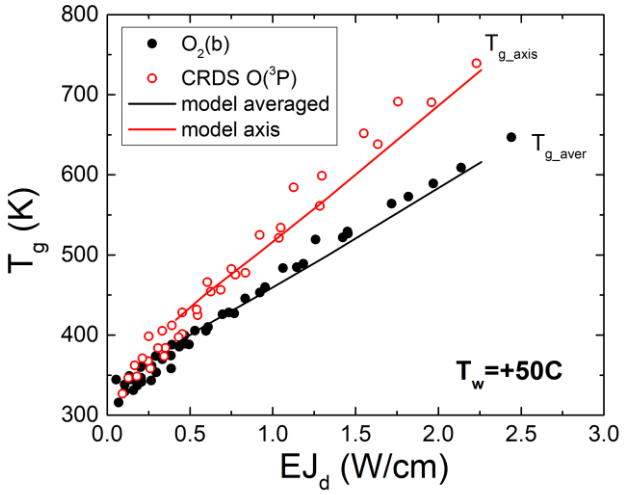

Figure 13. Gas temperature on the tube axis, Tg_{axis} (CRDS data) and average over the radial distribution of $O_2(b^1\Sigma_g^+)$, T_{g_aver} (OES data) depending on the applied linear power EJ_d.

The measured O(^{3}P) density is compared to the model in figure 14. Figure 14a shows the steady-state O(^{3}P) density at the axis as a function of pressure for different currents (10, 30 and 40 mA). Figure 14b shows O(^{3}P) density dynamics during partial modulation at 20 mA discharge current and pressure values of 1, 3, 8 Torr. The O(^{3}P) density is normalized to the value prior to the current drop. There is a good agreement between the model results and the experimental data.

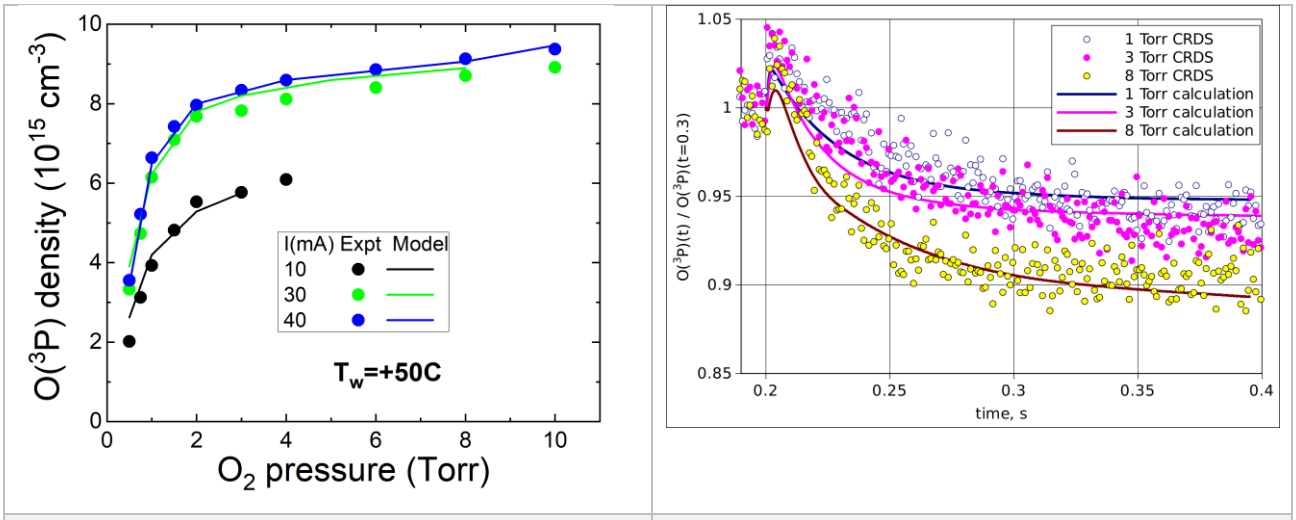

(a) (b)

Figure 14. Experimental data and model results on O(^{3}P): (a) Steady-state O(^{3}P) density at the discharge axis as a function of pressure, (b) O(^{3}P) density dynamics during partial current modulation at 20 mA (current decreases by 15% at 0.3 seconds) and pressures of 1, 3, 8 Torr.

5.2 $O_2(b^1\Sigma_g^+)$ kinetics: evidence for a reactive quenching process

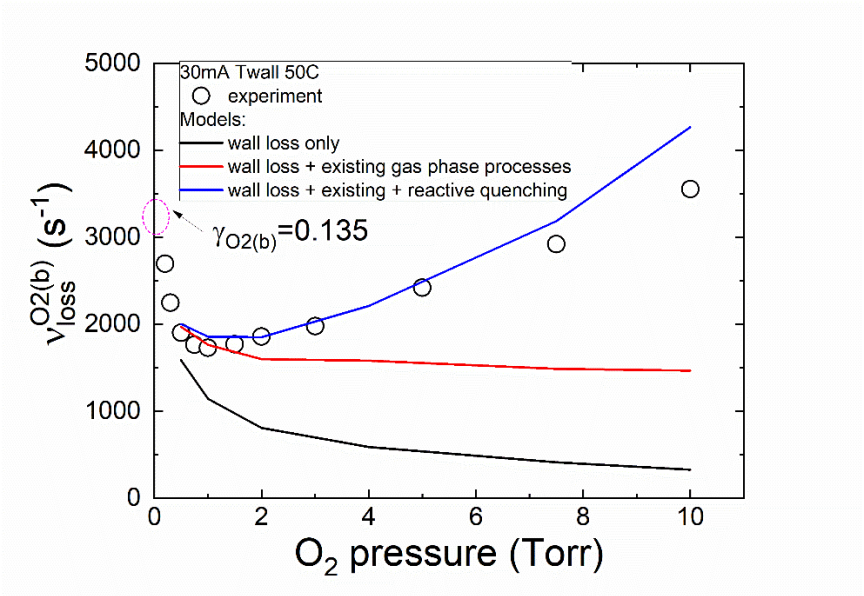

Figure 15. $O_2(b^1\Sigma_g^+)$ loss frequencies as a function of pressure at 30 mA. The symbols are experimental measurements, the lines are model results. The black line is for wall loss only, red is with wall loss and the existing reaction scheme for gas-phase processes, and the blue line is with the new reactive quenching process added.

Figure 15 compares the experimentally measured $O_2(b^1\Sigma_g^+)$ loss frequencies, $\nu_{loss}^{O2(b)}$, at 30 mA to different models. The black curve is a model including only wall loss, with a constant

surface loss probability of 0.135, calculated from the extrapolation of the experimental data to zero pressure. The red curve model additionally includes all currently-known gas-phase $O_2(b^1\Sigma_g^+)$ loss processes, but not the additional reactive quenching process, (R5). This model does not fit observed loss frequency for pressures higher than 2 Torr. The model including the reactive quenching process, (R5) is shown by the blue curve. For pressures above ~1 Torr, $O_2(b^1\Sigma_g^+)$ is mainly lost by volume reactions. The experimental results indicate the presence of a significant loss process for $O_2(b^1\Sigma_g^+)$ under conditions of high gas temperature and high $O(^3P)$ density, therefore we propose the addition of process R5:

$$O2(b^1\Sigma_g^+) + O(^3P) \rightarrow O_2(X^3\Sigma_g^-) + O(^3P),\ k_5=1\cdot10^{-10}\times\exp(-3700/T) \qquad (R5)$$

The model results with this additional process agree well with the experimentally observed $O_2(b^1\Sigma_g^+)$ loss frequencies as seen in figure 15. The need to consider not only previously-known collisional quenching (R4), but also reactive quenching with a significant activation energy barrier was pointed out by Volynets et al.[26]. In that study, the role of the reactive quenching of the $O_2(a^1\Delta_g)$ and $O_2(b^1\Sigma_g^+)$ states by oxygen atoms was investigated in a radiofrequency capacitively-coupled discharge at 81 MHz. The gas temperature in that system was hot, in the range 700 K - 1700, and possible mechanisms of this quenching process were considered. The reactive quenching of $O_2(a^1\Delta_g)$ was found to have a high energy barrier (in the range 0.55-0.69eV), which allowed the rate constant to be determined quite reliably in this temperature range. However, due to the lower energy barrier for the reactive quenching of $O_2(b^1\Sigma_g^+)$, accurate data can only be obtained at lower gas temperatures and under better-controlled conditions. In addition, it is necessary to know the absolute density of $O_2(b^1\Sigma_g^+)$ in order to estimate the rate constant.. Volynets et al. estimated that value of the quenching rate constant, k_5 of around $2\cdot10^{-11}\exp(-3700/T_g)$. However, it is likely that the $O_2(b^1\Sigma_g^+)$ density was overestimated in this work, due to the additional detection of nearby O atom emission lines. Furthermore, the $O_2(b^1\Sigma_g^+)$ spatial density profiles were not measured, so this value is likely to be an underestimate.

The current study concerns the lower temperature range of 300 to 700 K. In the model, the activation energy and pre-exponential factor in the quenching constant $k_5 = k_0\exp(-E_{act}/T_g)$ were varied over the ranges of E_{act} = (3600-3800) K and $k_0 = (5\cdot10^{-11}\text{-}1\cdot10^{-10})$ cm^3/s. The optimal values were derived from the best fitting of the simulation results to the experimental data. This range of activation energies is consistent with the reaction mechanism discussed by Volynets et al. For the experimental conditions studied here, the rate constant is more sensitive to changes in the pre-exponential factor. As discussed above, the optical emission data can lead to an overestimation of the $O_2(b^1\Sigma_g^+)$ concentration, especially under the high-pressure, high-power conditions of Volynets et al. where the emission intensity from other species (principally O atoms) was significantly higher than in our experiment. Therefore, the value $5\cdot10^{-11}$ cm^3/s was chosen as the lower limit of the pre-exponential factor. In addition, in the temperature range (300-500) K, collisional quenching of $O_2(b^1\Sigma_g^+)$ with a rate constant $k_4=(8\pm2)\cdot10^{-14}$ cm^3/s also plays a significant role. The temperature dependence of the rate constants for the processes (R4), (R5) and (R6) (solid lines) and the range of their variation (dashed lines) are shown in figure 16. The black dashed lines around the R5 line show the effect of varying the activation energy: E_{act} = 3600 K – upper dashed line, E_{act} = 3800 K – lower dashed line. The magenta dashed line shows the result obtained with the lowest value of the pre-exponential factor ($5\cdot10^{-11}$ cm^3/s). The temperature dependence of the total rate constant for $O_2(b^1\Sigma_g^+)$ quenching by $O(^3P)$ atoms ($k_4+k_5(T)$) is also shown in figure 16.

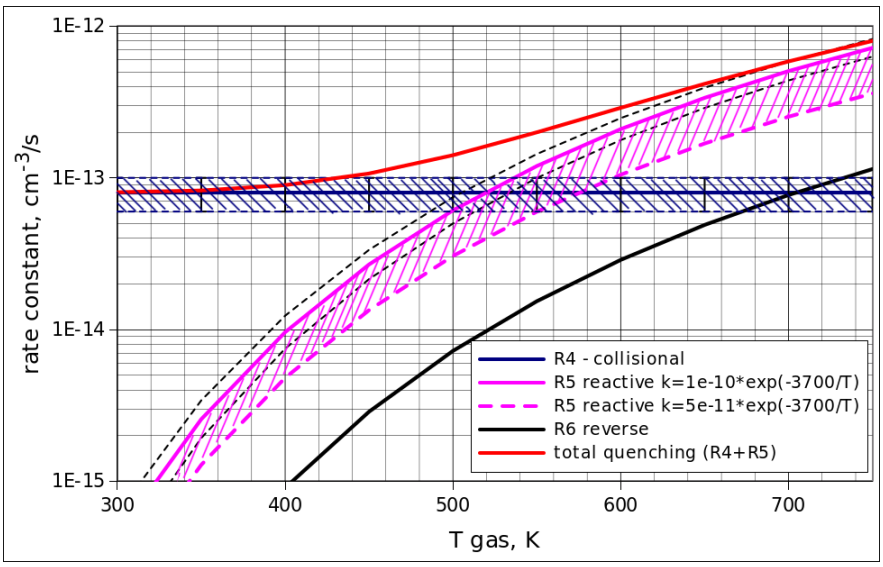

Figure 16. Temperature variation of the rate constants for different processes of $O_2(b^1\Sigma_g^+)$ quenching by O atoms (full lines: rate constants used in this work; the dashed lines and the shaded areas are the range of variation of the rate constants k4 and k5)

In the following the significant role of this additional reactive quenching will be illustrated by comparing the experimental and numerical results on the $O_2(b^1\Sigma_g^+)$ radial profile, the $O_2(b^1\Sigma_g^+)$ average density as a function of discharge pressure and current, as well as the $O_2(b^1\Sigma_g^+)$ density dynamics during modulation. For most calculations the values used are $k_4 = 8 \cdot 10^{-14}$ cm^3/s (previous literature value) and $k_5 = 1 \cdot 10^{-10} \exp(-3700/T_g)$. The result of varying these rate constants in the range shown in figure 16 will also be shown.

Figure 17 compares the measured and modeled time-variation of the $O_2(b^1\Sigma_g^+)$ density during current modulation at 30 mA and for pressures of 0.5, 2 and 5 Torr in figure 17a and for pressures of 1, 3 and 8 Torr in figure 17b. The blue lines are experimental data and red lines are model results. Good agreement between calculation and experimental results is found over the whole pressure range studied.

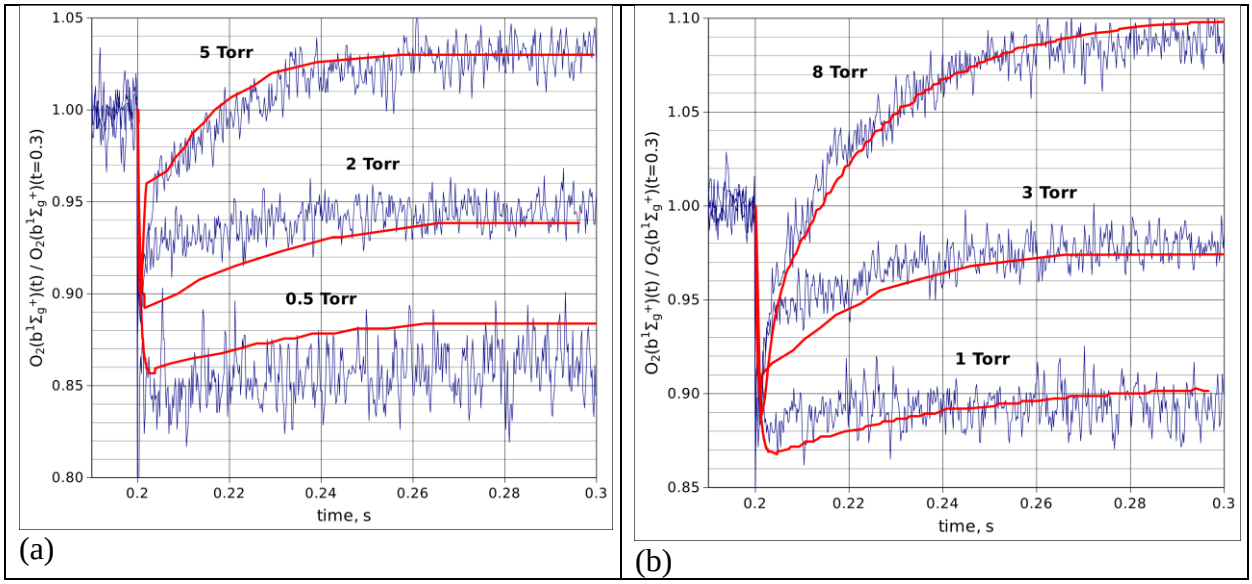

Figure 17. $O_2(b^1\Sigma_g^+)$ density dynamics during current modulation at 30 mA discharge current (the current decreases by ~15% at 0.3 seconds): experiment (blue curves) and model results (red curves), gas pressures values: (a) 0.5, 2, 5 Torr; (b) 1, 3, 8 Torr

To better illustrate the necessity to add reactive quenching to the model, figure 18 shows the time-variation of the $O_2(b^1\Sigma_g^+)$ density at 8 Torr, 30 mA. The red curve shows the model result without reactive quenching. The results obtained by varying rate constant of collisional quenching process, R4, are also shown by dashed blue lines (in this case the reactive quenching R5 was assumed to have a pre-exponential factor of $5 \cdot 10^{-11}$ for visual clarity of calculated curves).

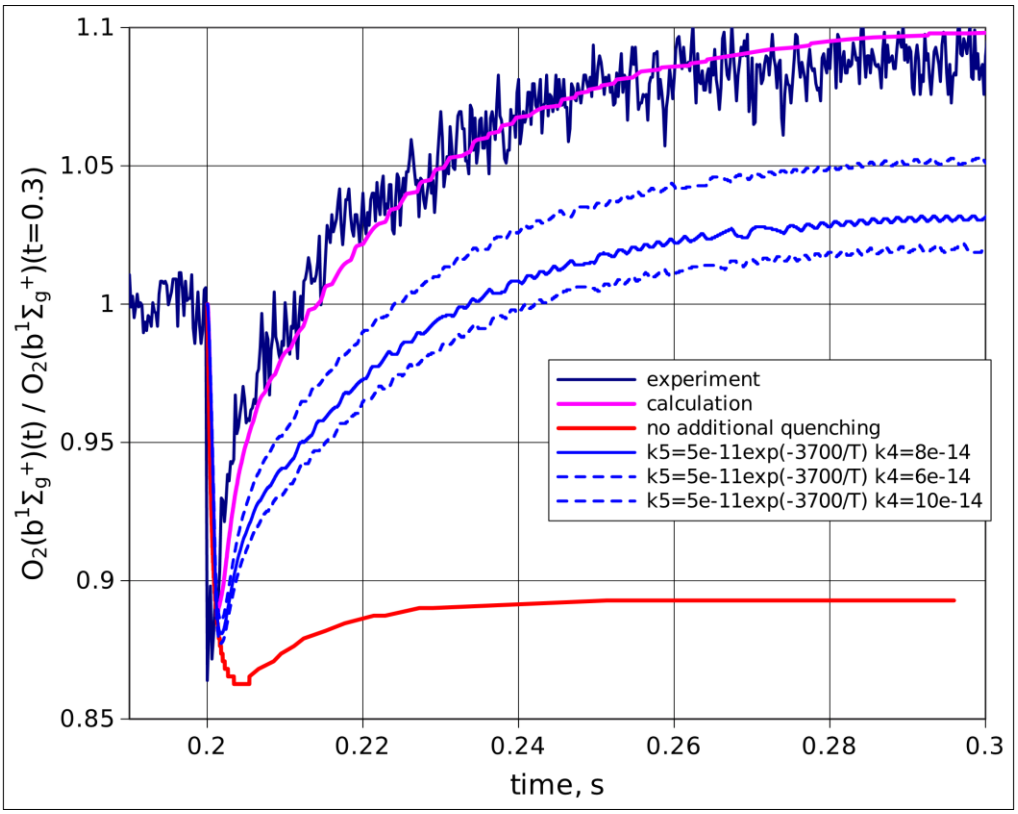

Figure 18. $O_2(b^1\Sigma_g^+)$ density dynamics at 8 Torr, 30 mA. The model results for different cases are shown: with no additional reactive quenching of $O_2(b^1\Sigma_g^+)$, and with different values of the rate constants for R4 and R5.

5.3 Radial profiles of the $O_2(b^1\Sigma_g^+)$ density

The radial profiles of the $O_2(b^1\Sigma_g^+)$ density for pressures of 1, 3 and 10 Torr are shown in figure 19a. The experimental measurements are shown by symbols, and the solid lines show model results (normalized to the experimental result at the reactor center). The measured $O_2(b^1\Sigma_g^+)$ density profile becomes flatter with increasing pressure. The model result at 10 Torr without additional reactive quenching is shown by a red curve, which clearly does not fit the observations. The additional quenching reaction (R5) causes flattening of the profiles at higher pressure. The gas temperature is higher at the discharge axis, leading to faster $O_2(b^1\Sigma_g^+)$ reactive quenching in this region. Figure 19b compares the 10 Torr experimental profile with models using different rates for reaction (R5), as well as varying the rate of collisional quenching (R4). The models using lower quenching rates cannot reproduce the observed flattened radial profile.

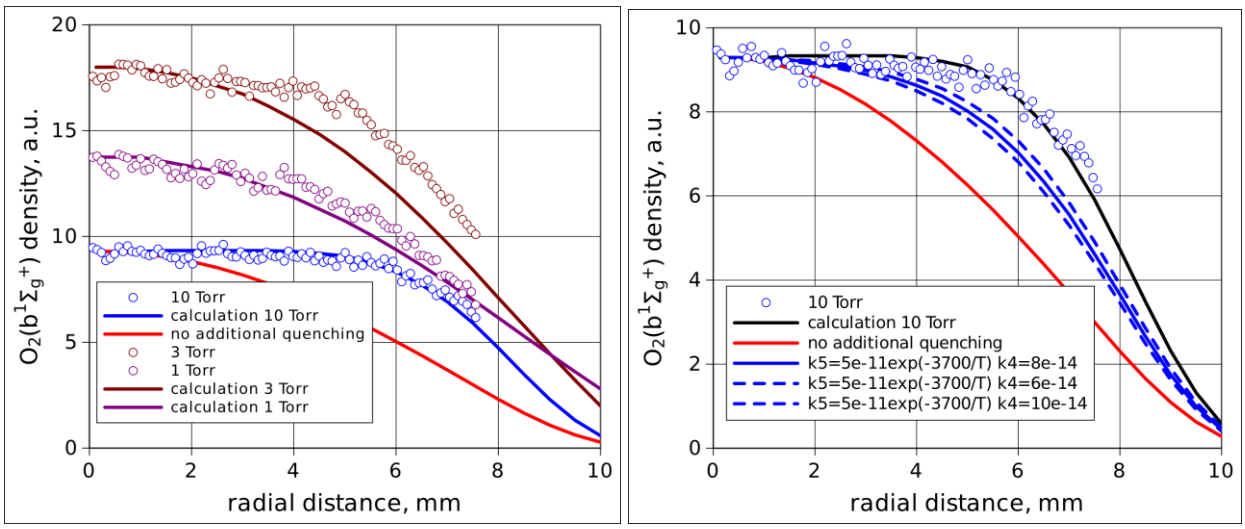

(a) (b)

Figure 19. $O_2(b^1\Sigma_g^+)$ radial profiles for 30 mA current, experimental and model results: (a) for pressures of 1, 3 and 10 Torr, (b) for 10 Torr with a variation of R4 and R5 rate constants.

5.4 $O_2(b^1\Sigma_g^+)$ density variation with pressure and current

The variation of the radially-averaged average $O_2(b^1\Sigma_g^+)$ density with pressure and current is shown in figure 20. Figure 20a shows the best model results for discharge currents 10, 30 and 40 mA. A separate red curve also presents the calculation without reactive quenching at 30 mA. The experimental trends with pressure and current are only reproduced when the additional reactive quenching (R5) process is included. The measured average $O_2(b^1\Sigma_g^+)$ density passes through a maximum at 2 Torr for currents of 20 mA and higher. The model also shows this behaviour, although the maximum occurs at slightly higher pressure. Without process (R5) the $O_2(b^1\Sigma_g^+)$ density increases continuously with pressure.

Figure 20b shows the measured average $O_2(b^1\Sigma_g^+)$ density (open and filled circles) as a function of pressure at 30 mA using the two different absolute calibration procedures described in the "Experiment" section. The open circles correspond to "absolutely calibrated OES measurements" and the full circles correspond to "VUV absorption measurements". The OES measurement gives $O_2(b^1\Sigma_g^+)$ densities higher by a factor of about 1.5. The simulation results with different values of the R4 and R5 rate constants are also shown in figure 20b. Above 2 Torr, using the additional reactive quenching R5 with a pre-exponential factor of $5{\cdot}10^{-11}$ agrees with the absolute OES measurements. Using R5 with a pre-exponential factor of $1{\cdot}10^{-10}$ agrees with the VUV measurements. It is worth noting that below 2 Torr, the gas temperature is low and reaction R5 has little effect on the $O_2(b^1\Sigma_g^+)$ loss. The $O_2(b^1\Sigma_g^+)$ production in this region is determined mainly by excitation transfer from $O(^1D)$ atoms to $O_2(X^3\Sigma_g^-)$ (see below). The rate of $O(^1D)$ production in the present model (R8 and R9) corresponds to the known literature data. This model cannot describe the observed density of $O_2(b^1\Sigma_g^+)$ obtained by OES at low pressures without an unrealistic change in the $O(^1D)$ production rate constants. This supports the VUV absorption measurements, along with a higher pre-exponential value of $1{\cdot}10^{-10}$ for the reaction R5.

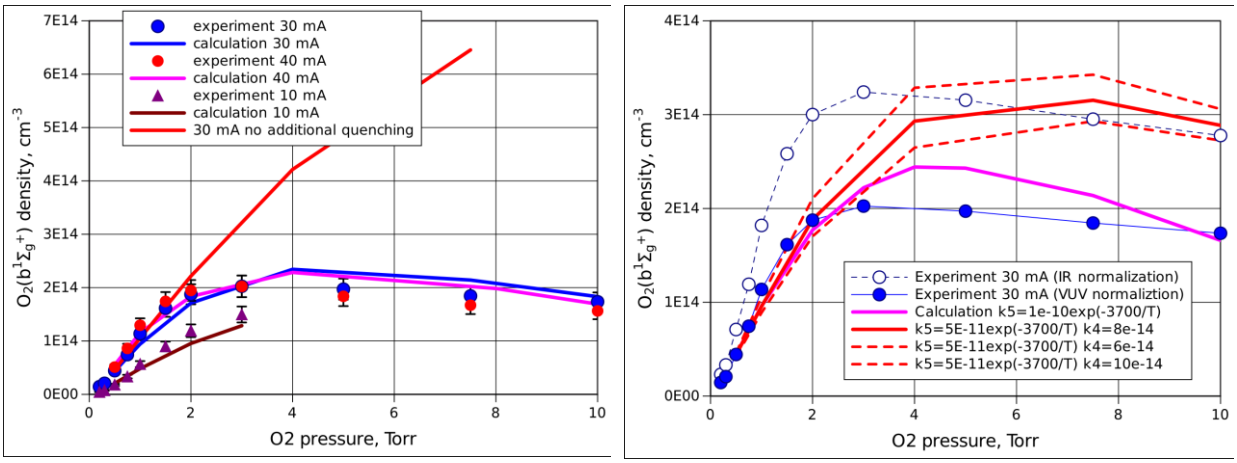

a) b)

Figure 20. $O_2(b^1\Sigma_g^+)$ density as a function of pressure: (a) for currents of 10, 30 and 40 mA with separate red curve shows the model result without R5 reaction for 30 mA; (b) for 30 mA discharge current. Experimental results for two different normalization and model results for R4, R5 rate variation are shown.

5.5 Relative importance of different $O_2(b^1\Sigma_g^+)$ production and loss processes

The (radially-averaged) fractional contributions of the different production and loss processes of $O_2(b^1\Sigma_g^+)$ are shown respectively in figure 21a and figure 21b as a function of pressure at 30 mA current. The dominant $O_2(b^1\Sigma_g^+)$ production channel is energy transfer from $O(^1D)$ to $O_2(X^3\Sigma_g^-)$ (R1), which produces over half of the $O_2(b^1\Sigma_g^+)$ at all pressures. The next most important channel is electron-impact excitation from $O_2(a^1\Delta_g)$ (R3), which contributes from 10 to 20% with increasing pressure. Excitation from the ground state (R2) becomes more significant with pressure, increasing from 5 to 20%.

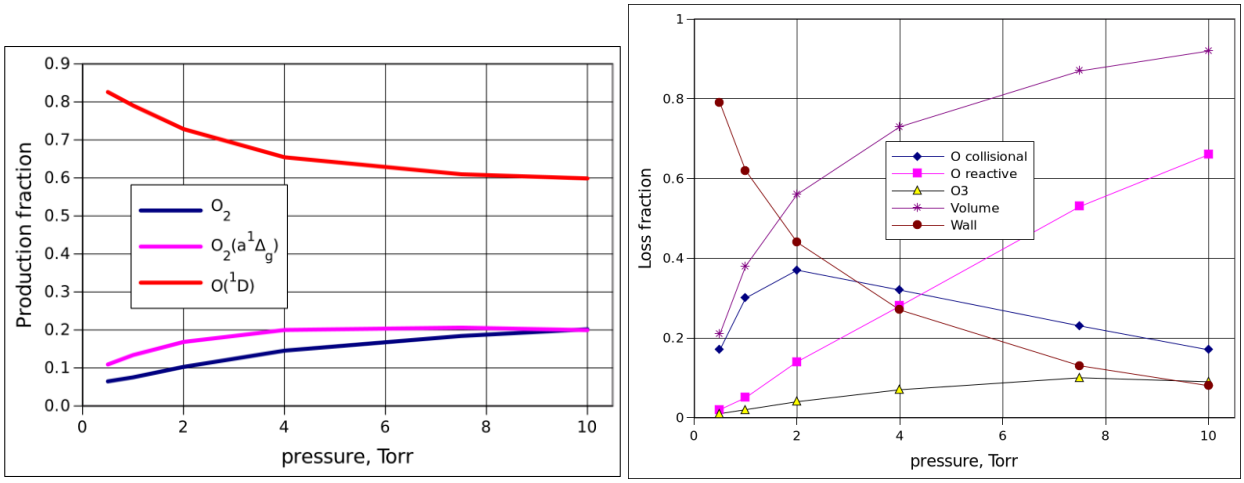

(a) (b)

Figure 21. (a) radially averaged production fractions of $O_2(b^1\Sigma_g^+)$ through different processes, as a function of pressure at current of 30 mA, (b) radially averaged $O_2(b^1\Sigma_g^+)$ loss fractions for different processes as a function of pressure at 30mA.

Concerning the loss processes of $O_2(b^1\Sigma_g^+)$, surface quenching is dominant at low pressure, but volume loss processes take over above 2 Torr. The contribution of reactive quenching (R5)

increases with pressure (due to the higher oxygen atom density and gas temperature), reaching 65% at 10 Torr. The rate of reaction with ozone (R7) also increases with pressure, reaching almost 10% at 10 Torr.

The calculated radial profiles of the $O_2(b^1\Sigma_g^+)$ loss rate due to reactions R4, R5, R7 are shown in Figures 22a, 22b and 22c for pressures of 0.5, 2 and 10 Torr, respectively. At 0.5 Torr, reaction R4 dominates the volume loss. At the intermediate pressure of 2 Torr, the rate of R5 reaction becomes comparable to that of R4 near the axis, but decreases towards the walls by two orders of magnitude due to the temperature gradient. At 10 Torr, reaction reactive quenching dominates up to a radius of r=0.7 cm, whereupon the reaction with ozone (R7) becomes dominant in the vicinity of the wall.

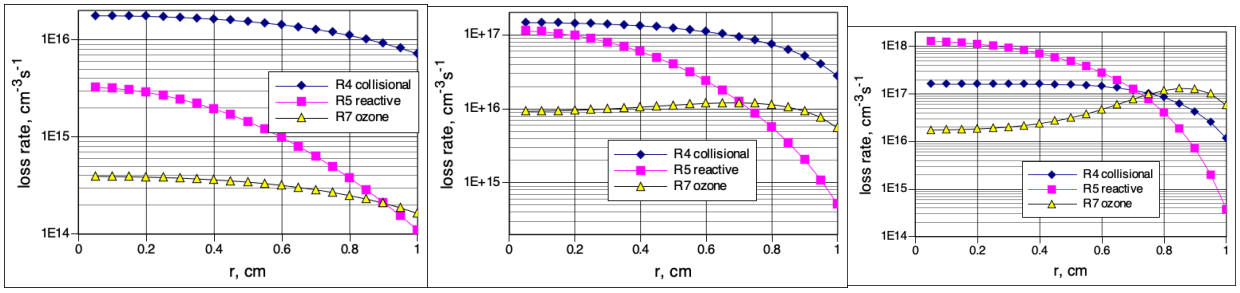

(a) (b) (c)

Figure 22. Radial profile of $O_2(b^1\Sigma_g^+)$ loss rate in reactions R4-"collisional", R5 – "reactive" and R7- "ozone" for current of 30 mA and pressures of (a) 0.5 Torr, (b) 2 Torr, (c) 10 Torr.

6. Conclusion

The density and kinetics of $O_2(b^1\Sigma_g^+)$ in a DC positive column discharge has been studied experimentally under well-controlled conditions. Comparison of the experimental results to numerical simulations of the $O_2(b^1\Sigma_g^+)$ radial profiles, the $O_2(b^1\Sigma_g^+)$ average density variation with pressure and current, and the $O_2(b^1\Sigma_g^+)$ density dynamics during current modulation indicated the existence of a fast quenching process of $O_2(b^1\Sigma_g^+)$ molecules by $O(^3P)$ atoms with a significant activation energy barrier. Measurements were carried out in a DC discharge in pure oxygen in the range of 0.5-10 Torr pressures and currents of 10–40 mA. This made it possible to study the temperature dependences of the rate constants over the gas temperature range Tg = 320–700 K. The density and temperature of $O(^3P)$ atoms were determined by time-resolved sub-Doppler CRDS of the $O(^3P_2) \rightarrow O(^1D_2)$ transition at 630 nm. The optical emission of $O_2(b^1\Sigma_g^+)$ at 762 nm was absolutely calibrated by direct measurements of the integral absolute intensity of the band $O_2(b^1\Sigma_g^+,v=0) \rightarrow O_2(X^3\Sigma_g^-,v=0)$. Additionally, the absolute $O_2(b^1\Sigma_g^+)$ density was confirmed by VUV absorption measurements [30]. The kinetics of $O_2(b^1\Sigma_g^+)$ and $O(^3P)$ were measured during partial modulation of the discharge current. The experiments show that the rate of $O_2(b^1\Sigma_g^+)$ quenching by $O(^3P)$ atoms rises rapidly with a gas temperature above ~ 450K.

The experimental results were analyzed by comparison with a self-consistent 1D model of the DC discharge. The entire set of experimental data can only be described by the model by including a reactive quenching process (R5) with an activation energy, Ea/k ~3700 K. Under the conditions studied here the gas temperature is small compared to 3700 K, so the results are more sensitive to changes in the pre-exponential factor. The relative contributions of the different $O_2(b^1\Sigma_g^+)$ loss processes were investigated using the model. At gas pressures below 2 Torr surface loss is dominant. The previously-known collisional quenching reaction (R4) prevails in the pressure range of 2 Torr < p < 4 Torr. The new reactive quenching process (R5) becomes the main loss channel above 4 Torr and 20 mA, when the gas temperature rise becomes significant.

The good agreement of the model and experimental results allows the rate constant of $O_2(b^1\Sigma_g^+)$ quenching by $O(^3P)$ atoms to be determined with reasonable accuracy. The best fit of the model results to the whole set of experimental data ($O_2(b^1\Sigma_g^+)$ radial profiles, $O_2(b^1\Sigma_g^+)$ density dependencies on pressure and current and the $O_2(b^1\Sigma_g^+)$ density dynamics during current modulation) is obtained with a rate constant $k_5=10^{-10}\cdot\exp(-3700/T)$ cm^3/s with an accuracy better than 20% over the whole range of discharge conditions studied.

Acknowledgements

This study was supported by the Russian Science Foundation, project no. 21-72-10040. D. Lopaev, S. Zyryanov, T. Rakhimova, and D. Voloshin would like to acknowledge the Interdisciplinary Scientific and Educational School of Moscow University "Photonic and Quantum Technologies. Digital Medicine". A. Chukalovsky, and Yu. Mankelevich would like to acknowledge the Interdisciplinary Scientific and Educational School of Moscow University "Fundamental and applied space research".

References

[1] Graves D B 2012 *Journal of Physics D: Applied Physics* **45** 263001
[2] Adamovich I et al. 2017 *Journal of Physics D: Applied Physics* **50** 323001
[3] Kylián O and Rossi F 2009 *Journal of Physics D: Applied Physics* **42** 085207
[4] Rich S A, Mille V, Vivien C, Godey S and Supiot P 2010 *Plasma Processes and Polymers* **7** 775-784
[5] Kogelschatz U 2003 *Plasma Chemistry and Plasma Processing* **23** 1-46
[6] Braginsky O V, Kovalev A S, Lopaev D V, Proshina O V, Rakhimova T V, Rakhimov A T and Vasilieva A N 2008 *Journal of Physics D: Applied Physics* **41** 172008
[7] Ionin A A, Kochetov I V, Napartovich A P and Yuryshev N N 2007 *Journal of Physics D: Applied Physics* **40** R25-R61
[8] Carroll D L, Benavides G F, Zimmerman J W, Woodard B S, Day M T, Palla A D, Verdeyen J T and Solomon W C "Enhanced performance of an electric oxygen-iodine laser" *Proc.SPIE* 2010.
[9] Hicks A, Tirupathi S, Jiang N, Utkin Y, Lempert W R, Rich J W and Adamovich I V 2007 *Journal of Physics D: Applied Physics* **40** 1408-1415
[10] Azyazov V N, Torbin A P, Pershin A A, Mikheyev P A and Heaven M C 2015 *Chemical Physics* **463** 65-69
[11] Heaven M C 2010 *Laser & Photonics Reviews* **4** 671-683
[12] Starikovskiy A and Aleksandrov N 2013 *Progress in Energy and Combustion Science* **39** 61-110
[13] Ju Y and Sun W 2015 *Combustion and Flame* **162** 529-532
[14] Starik A M, Loukhovitski B I, Sharipov A S and Titova N S 2015 *Philos Trans A Math Phys Eng Sci* **373**
[15] Starik A M, Kuleshov P S and Titova N S 2009 *Journal of Physics D: Applied Physics* **42** 175503
[16] Fridman G, Friedman G, Gutsol A, Shekhter A B, Vasilets V N and Fridman A 2008 *Plasma Processes and Polymers* **5** 503-533
[17] Weltmann K D and von Woedtke T 2016 *Plasma Physics and Controlled Fusion* **59** 014031
[18] Gousset G, Ferreira C M, Pinheiro M, Sa P A, Touzeau M, Vialle M and Loureiro J 1991 *Journal of Physics D: Applied Physics* **24** 290-300
[19] Kossyi I A, Kostinsky A Y, Matveyev A A and Silakov V P 1992 *Plasma Sources Science and Technology* **1** 207-220
[20] Lee C, Graves D B, Lieberman M A and Hess D W 1994 *Journal of The Electrochemical Society* **141** 1546-1555

[21] Gordiets B F, Ferreira C M, Guerra V L, Loureiro J M A H, Nahorny J, Pagnon D, Touzeau M and Vialle M 1995 *IEEE Transactions on Plasma Science* **23** 750-768
[22] Stafford D S and Kushner M J 2004 *Journal of Applied Physics* **96** 2451-2465
[23] Gudmundsson J T 2004 *Journal of Physics D: Applied Physics* **37** 2073-2081
[24] Braginskiy O V, Vasilieva A N, Klopovskiy K S, Kovalev A S, Lopaev D V, Proshina O V, Rakhimova T V and Rakhimov A T 2005 *Journal of Physics D: Applied Physics* **38** 3609-3625
[25] Annušová A, Marinov D, Booth J-P, Sirse N, da Silva M L, Lopez B and Guerra V 2018 *Plasma Sources Science and Technology* **27** 045006
[26] Volynets A V, Lopaev D V, Rakhimova T V, Proshina O V, Chukalovsky A A and Booth J P 2020 *Plasma Sources Science and Technology* **29** 115020
[27] Booth J-P, Chatterjee A, Guaitella O, Lopaev D, Zyryanov S, Rakhimova T, Voloshin D, Oliveira N and Nahon L "Filling the Gaps in Our Understanding of Plasmas in Simple Diatomic Gases-Combining a DC Plasma in Pure O2 with Multiple Advanced Diagnostics for Experimental Validation of Simulations" *ISPlasma2021/IC-PLANTS2021*. Nagoya, Japan 2021.
[28] Booth J P, Guaitella O, Chatterjee A, Drag C, Guerra V, Lopaev D, Zyryanov S, Rakhimova T, Voloshin D and Mankelevich Y 2019 *Plasma Sources Science and Technology* **28** 055005
[29] Booth J-P et al. 2020 *Plasma Sources Science and Technology* **29** 115009
[30] Western C, Booth J-P, Chatterjee A and De Oliveira N 2021 *Molecular Physics* **119** e1741714
[31] Peverall R, Rogers S D A and Ritchie G A D 2020 *Plasma Sources Science and Technology* **29** 045004
[32] Raizer Y P *Gas Discharge Physics*: Springer Berlin, Heidelberg, 1991
[33] Westenberg A A and de Haas N 1963 *Phys. Fluids* **6** 617
[34] Burcat A and Ruscic B "*Third millenium ideal gas and condensed phase thermochemical database for combustion (with update from active thermochemical tables)"* Technical report ANL-05/20; TAE 960 Argonne National Laboratory 2005 United States
[35] Kovalev A, Lopaev D, Mankelevich Y A, Popov N, Rakhimova T, Poroykov A Y and Carroll D 2005 *J. Phys. D: Appl. Phys* **38** 2360-2370
[36] Vasiljeva A N, Klopovskiy K S, Kovalev A S, Lopaev D V, Mankelevich Y A, Popov N A, Rakhimov A T and Rakhimova T V 2004 *Journal of Physics D: Applied Physics* **37** 2455-2468
[37] Ivanov V V, Klopovsky K S, Lopaev D V, Rakhimov A T and Rakhimova T V 1999 *IEEE Transactions on plasma science* **27** 1279-1287
[38] Lawton S and Phelps A 1978 *The Journal of Chemical Physics* **69** 1055-1068
[39] Streit G E, Howard C J, Schmeltekopf A L, Davidson J A and Schiff H I 1976 *The Journal of Chemical Physics* **65** 4761-4764
[40] Slanger T G and Black G 1979 *The Journal of Chemical Physics* **70** 3434-3438
[41] Lee L C and Slanger T G 1978 *The Journal of Chemical Physics* **69** 4053-4060
[42] Young R A and Black G 1967 *The Journal of Chemical Physics* **47** 2311-2318
[43] Taniguchi N, Hirai K, Takahashi K and Matsumi Y 2000 *The Journal of Physical Chemistry A* **104** 3894-3899
[44] Takahashi K, Takeuchi Y and Matsumi Y 2005 *Chemical Physics Letters* **410** 196-200
[45] Grondin R, Loison J-C and Hickson K M 2016 *The Journal of Physical Chemistry A* **120** 4838-4844
[46] Miura N, Hashimoto K, Takahashi K, Taniguchi N and Matsumi Y 2002 *The Journal of Chemical Physics* **116** 5551-5556
[47] Grebenshchikov S Y, Qu Z-W, Zhu H and Schinke R 2007 *Physical Chemistry Chemical Physics* **9** 2044-2064

[48] Pejaković D A, Copeland R A, Slanger T G and Kalogerakis K S 2014 *The Journal of chemical physics* **141** 024303
[49] Gauthier M and Snelling D 1971 *The Journal of Chemical Physics* **54** 4317-4325
[50] Snelling D 1974 *Canadian Journal of Chemistry* **52** 257-270
[51] McCullough D and McGrath W 1972 *Journal of Photochemistry* **1** 241-253
[52] Dunlea E J and Ravishankara A 2004 *Physical Chemistry Chemical Physics* **6** 2152-2161
[53] Strekowski R, Nicovich J and Wine P 2004 *Physical Chemistry Chemical Physics* **6** 2145-2151
[54] Blitz M A, Dillon T J, Heard D E, Pilling M J and Trought I D 2004 *Physical Chemistry Chemical Physics* **6** 2162-2171
[55] Slanger T G, Hwang E S, Bartlett N C-M and Kalogerakis K S 2018 *The Journal of Physical Chemistry A* **122** 8114-8125
[56] Atkinson R, Baulch D L, Cox R A, Jr. R F H, Kerr J A, Rossi M J and Troe J 1997 *Journal of Physical and Chemical Reference Data* **26** 521-1011
[57] Middleton A, Teubner P and Brunger M 1992 *Physical review letters* **69** 2495
[58] Tashiro M, Morokuma K and Tennyson J 2006 *Physical Review A* **73** 052707
[59] Hall R I and Trajmar S 1975 *Journal of Physics B: Atomic and Molecular Physics* **8** L293-L296
[60] Laher R R and Gilmore F R 1990 *Journal of Physical and Chemical Reference Data* **19** 277-305
[61] Zatsarinny O and Tayal S 2003 *The Astrophysical Journal Supplement Series* **148** 575
[62] Yee J H, Guberman S L and Dalgarno A 1990 *Planetary and Space Science* **38** 647-652
[63] Abreu V J, Yee J H, Solomon S C and Dalgarno A 1986 *Planetary and Space Science* **34** 1143-1145
[64] Doroshenko V M, N K N and V S V 1992 *Khimiya Vysokikh Energii* **26** 291
[65] Borrell P M, Borrell P, Grant K R and Pedley M D 1982 *The Journal of Physical Chemistry* **86** 700-703
[66] Zagidullin M V, Khvatov N A, Medvedkov I A, Tolstov G I, Mebel A M, Heaven M C and Azyazov V N 2017 *The Journal of Physical Chemistry A* **121** 7343-7348
[67] Zinn J, Sutherland C, Stone S, Duncan L and Behnke R 1982 *Journal of Atmospheric and Terrestrial Physics* **44** 1143-1171
[68] Xie W, Liu L, Sun Z, Guo H and Dawes R 2015 *The Journal of Chemical Physics* **142** 064308